Theses and Dissertations   Thesis and Dissertation Collection

1988-06

Radiation effects on rare earth permanent magnets

Luna, Henry Buenviaje

NAVAL POSTGRADUATE SCHOOL
Monterey , California

THESIS

RADIATION EFFECTS ON RARE EARTH
PERMANENT MAGNETS

by

Henry Buenviaje Luna

June 1988

Thesis Advisor	X.K. Maruyama
Co-Advisor	N.J. Colella

Approved for public release; distribution is unlimited.

REPORT DOCUMENTATION PAGE

1a Report Security Classification Unclassified		1b Restrictive Markings			
2a Security Classification Authority		3 Distribution Availability of Report			
2b Declassification Downgrading Schedule		Approved for public release; distribution is unlimited.			
4 Performing Organization Report Number(s)		5 Monitoring Organization Report Number(s)			
6a Name of Performing Organization Naval Postgraduate School	6b Office Symbol (if applicable) 33	7a Name of Monitoring Organization Naval Postgraduate School			
6c Address (city, state, and ZIP code) Monterey, CA 93943-5000		7b Address (city, state, and ZIP code) Monterey, CA 93943-5000			
8a Name of Funding Sponsoring Organization	8b Office Symbol (if applicable)	9 Procurement Instrument Identification Number			
8c Address (city, state, and ZIP code)		10 Source of Funding Numbers			
		Program Element No	Project No	Task No	Work Unit Accession No

11 Title (include security classification) RADIATION EFFECTS ON RARE EARTH PERMANENT MAGNETS

12 Personal Author(s) Henry Buenviaje Luna

13a Type of Report Master's Thesis	13b Time Covered From To	14 Date of Report (year, month, day) June 1988	15 Page Count 95

16 Supplementary Notation The views expressed in this thesis are those of the author and do not reflect the official policy or position of the Department of Defense or the U.S. Government.

17 Cosati Codes			18 Subject Terms (continue on reverse if necessary and identify by block number)
Field	Group	Subgroup	REPMs, LLNL's LINAC, magnetic properties, ITS/CYLTRAN

19 Abstract (continue on reverse if necessary and identify by block number)

With continuing improvements in rare earth permanent magnet (REPM) technology, applications for their use are being discovered that were previously not possible. Two such applications for permanent magnets are in focusing elements for linear accelerators and ion sources, and in insertion devices (wigglers and undulators) used to produce synchrotron radiation. However, these magnetic transport elements are subjected to high radiation levels. Consequently, there is considerable interest in the United States and abroad to discover and quantify the effects of radiation on REPMs. Using the Lawrence Livermore National Laboratory (LLNL) 100 MeV Linac, four different samples of REPM were irradiated to one to two gigarads of exposed dose from a bremsstrahlung production target in an attempt to simulate the consequences of beam spills of a high energy primary electron beam. Of the samples irradiated, Sm_2Co_1 proved to be the most resistant to gamma radiation. The electron transport code CYLTRAN of the Integrated Tiger Series (ITS), which is an electron and photon Monte Carlo simulation code, was used to determine the angular and energy spectra for both electrons and photons produced by the target used at the LLNL Linac.

20 Distribution Availability of Abstract ☒ unclassified unlimited ☐ same as report ☐ DTIC users	21 Abstract Security Classification Unclassified	
22a Name of Responsible Individual X K. Maruyama	22b Telephone (include Area code) (408) 646-2431	22c Office Symbol 61Mx

DD FORM 1473,84 MAR	83 APR edition may be used until exhausted All other editions are obsolete	security classification of this page

Radiation Effects on Rare Earth Permanent Magnets

by

Henry Buenviaje Luna
Lieutenant, United States Navy
B.S., United States Naval Academy, 1979

Submitted in partial fulfillment of the
requirements for the degree of

MASTER OF SCIENCE IN PHYSICS

from the

NAVAL POSTGRADUATE SCHOOL
June 1988

ABSTRACT

With continuing improvements in rare earth permanent magnet (REPM) technology, applications for their use are being discovered that were previously not possible. Two such applications for permanent magnets are in focusing elements for linear accelerators and ion sources, and in insertion devices (wigglers and undulators) used to produce synchrotron radiation. However, these magnetic transport elements are subjected to high radiation levels. Consequently, there is considerable interest in the United States and abroad to discover and quantify the effects of radiation on REPMs. Using the Lawrence Livermore National Laboratory (LLNL) 100 MeV Linac, four different samples of REPM were irradiated to one to two gigarads of exposed dose from a bremsstrahlung production target in an attempt to simulate the consequences of beam spills of a high energy primary electron beam. Of the samples irradiated, Sm_2Co_{17} proved to be the most resistant to gamma radiation. The electron transport code CYLTRAN of the Integrated Tiger Series (ITS), which is an electron and photon Monte Carlo simulation code, was used to determine the angular and energy spectra for both electrons and photons produced by the target used at the LLNL Linac.

TABLE OF CONTENTS

LIST OF TABLES

LIST OF TABLES

LIST OF FIGURES

ACKNOWLEDGEMENTS

I. INTRODUCTION

The development of permanent magnet materials has progressed tremendously since the beginning of this century. However, new to technology then, permanent magnets gave a relatively low performances in most technological applications. As a result, electromagnets were preferred. With steady increase in quality and performance, permanent magnets are supplanting electromagnets for many applications. Today permanent magnets are so widely used that one could consider them as an indispensable prerequisite of modern technology. By far the largest application of permanent magnets is in motors and generators. Next in importance are telecommunication, data manipulations and for measurement and control applications. Substantial numbers of permanent magnets are also used in acoustic devices and magnetomechanical applications. [Ref. 1: p. 11]

The application depends on the quality or strength of the permanent magnet. A measure of quality for permanent magnets is the maximum energy product $(BH)_{max}$ occuring in the magnetic hysteresis loop. The maximum energy product is commonly expressed in megagauss-oersteds (MGOe). In the SI unit system, $(BH)_{max}$ is measured in kJ m³, where one MGOe equals 7.96 kJ/m³. An ideal permanent magnet would have a constant magnetization equal to the saturation magnetization M_s in any applied field. If pure iron could be made into an ideal permanent magnet with 100 percent density, it would have an energy product of 107 MGOe [Ref. 1: p. 11]. This is considered to be the maximum energy product achievable in a magnetic material. Appendix A provides detailed descriptions of magnetic properties of materials and Appendix B is a glossary of common terms associated with magnetic properties of materials.

Since the mid 1960's, improvements in rare earth permanent magnet (REPM) technology have shown remarkable progress [Ref. 2: p. 1]. Figure 1 on page 2 shows the historical development of the energy product quantity. Improvements in the quality of compounds of rare earth materials such as samarium-cobalt (Sm-Co) and more recently compounds of neodymium, iron and boron (Nd-Fe-B) have provided new applications that were previously not possible. The use of REPMs in accelerator applications include magnetic focusing devices for linear accelerators and ion sources, and insertion devices (wigglers and undulators) for synchrotron radiation sources. These applications have evoked considerable interest in permanent magnets both in the United States and
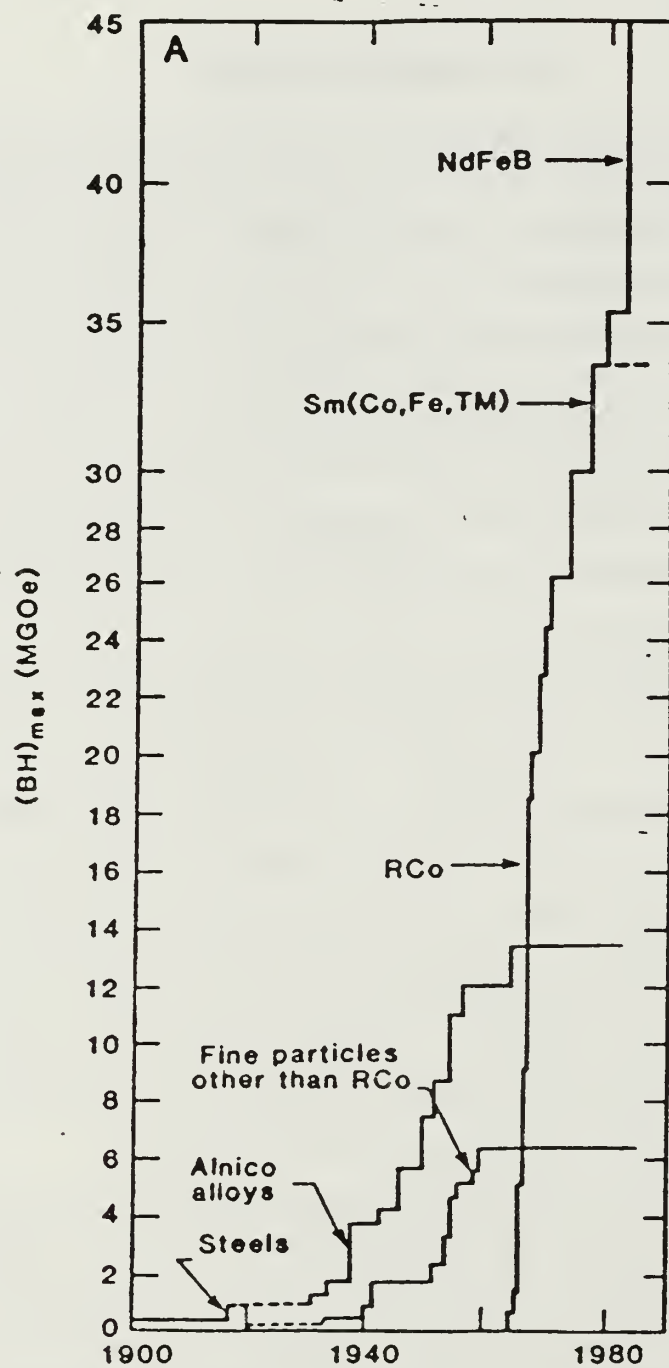
Figure 1. Improvements in Magnetic Quality of Permanent Magnets

abroad. These materials are characterized by a high remanent induction B_r and high coercive force H_c which are used to produce high multipole fields in extremely compact magnets. These applications often require the magnets to operate in high radiation environments.

Although many magnetic properties of REPM materials have been studied, to date the understanding of the effects of ionizing radiation is phenomenological at best. Previous studies have focused mostly on determining the effects of exposing REPM samples to beams of protons and fission neutrons. However, the permanent magnet components of a wiggler in free electron laser (FEL) systems can be expected to receive very potentially high doses of secondary electron and photon radiation. High radiation levels can be produced from electrons that are lost from a primary beam due to accidental beam spillage, poor emittance, or improper front-end matching. The lost electrons interact with the beam pipe producing a mixed field of radiation, including bremsstrahlung photons, a fission-like spectrum of neutrons and a broad distribution in energy of electrons [Ref. 3: p. 2]. Experiments were conducted at the Linear Accelerator (Linac) at Lawrence Livermore National Laboratory (LLNL) to determine which commercially available permanent magnet alloys are the most insensitive in their magnetic properties to high levels of this type of radiation environment.

The Integrated Tiger Series (ITS), a Monte-Carlo simulation code developed to study the manner in which electrons and photons propagate through materials, was used to determine electron and photon energy and angular spectra of radiation produced by the target at LLNL's Linac. The ITS Monte-Carlo scheme calculates a particle's energy, direction and position at discrete intervals as the particle travels through a material. Energy deposition and ionizing levels are computed. Total dose in any material can then be calculated.

The ITS code CYLTRAN simulates the transport of electrons and photons through a cylindrical geometry. The beam production target and experimental setup at LLNL's Linac were modeled using CYLTRAN. Results from the simulation codes were compared with experimental data and are discussed in Chapter IV.

II. BACKGROUND

In our experiment conducted at the 100 MeV Linac Facility at LLNL, studies were made to measure the effects on high levels of gamma radiation on rare earth permanent magnets. Other experiments dating back to July, 1982 were conducted by other laboratory groups. These experiments however, were focused on radiation effects on magnets exposed to high fluences of protons and neutrons.

In 1982, radiation effects on Sm-Co permanent magnets were studied at Los Alamos National Laboratory (LANL). Samples of $SmCo_5$ (Hicorex 90B) and $(SmPr)Co_5$ (Hicorex 96B) manufactured by Hitachi Magnetics were irradiated by neutrons produced at the Los Alamos Meson Production Facility (LAMPF). The neutrons were produced by the interaction of the LAMPF 800 MeV proton beam with various isotope production targets. A maximum neutron fluence of 1.1×10^{18} n/cm^2 was deposited on each magnet. A two percent drop in magnetic remanence was measured after the irradiation. Temperatures for the $SmCo_5$ and $(SmPr)Co_5$ samples were monitored with thermocouples positioned near each sample. The maximum temperature recorded was 140 °C at maximum proton beam current. Since the stabilizing temperature on these magnets were designed at 100 °C, the studies concluded that the decrease in remanence was consistent with thermally induced demagnetization. No clear conclusions were made in this experiment to what effects the radiation had on the Sm-Co magnets. [Ref. 2: pp. 4-6]

In 1983, studies on proton radiation effects on rare earth cobalt (REC) permanent magnets were conducted at CERN. These studies were designed to examine radiation effects on the relatively high remanent induction B_r and high coercive force H_c magnets used for particle beam transport elements such as quadrupoles and sextupoles. However little was known about the radiation resistance of RECs. Numerous applications of REC magnets at CERN made necessary studies in this area. Four different samples of Sm-Co were irradiated. The magnets used were two samples of $SmCo_5$ (Vacomax 200 and Koermax 160), one sample of Sm_2Co_{17} and the fourth sample was a composite material composed of 65.6 percent copper, 24.1 percent samarium and 10.3 percent composite of other various rare earth metals (Recoma 20). The energy of the incident proton beam used to irradiate the magnet samples was 400 GeV. A total dose of 11.4 gigarads was deposited on the $SmCo_5$ (Koermax 160) sample, and 10.5 gigarads on the Sm_2Co_{17}

sample. An unexpectedly high loss in remanence was found on all samples with the exception of Sm_2Co_{17}. The Sm_2Co_{17} sample, which received a dose of 10.5 gigarads, suffered a three percent loss in remanence. The $SmCo_5$ (Koermax 160) sample received a total dose of 11.4 gigarads and suffered a much greater loss in remanence, 24.2 percent [Ref. 4: p. 10]. Thermal effect studies were performed prior to irradiation to demonstrate that a loss in remanence was not caused by excessive temperature. Magnet samples were heated to 90 °C for 120 hours in an oven and the measured magnetization loss was less than 0.25 percent. During irradiation, the temperature fluctuated between 30 °C and 80 °C. According to manufacturer specifications, the demagnetization effect at these temperatures was less than one percent. Therefore, it was concluded that there was no significant loss due to temperature [Ref. 4: p. 3].

A similar study was performed at TRIUMPF, in Vancouver, B.C. in 1985. Like the study performed at CERN, Sm-Co permanent magnets were being used extensively in radiation environments. Four samples of different Sm-Co compounds and one sample of Nd-Fe-B were irradiated with a 500 MeV proton beam. Hitachi Magnetics Corporation supplied samples of $SmCo_5$ (Hicorex 90B) and $(SmPr)Co_5$ (Hicorex 96B). Crucible Magnetics supplied another sample of $SmCo_5$ (Crucore 18) and Sm_2Co_{17} (Crucore 26). The Nd-Fe-B samples were supplied by IG Technologies (NeIGT 27). After receiving a total proton dose of 12 gigarads, Crucore 26, a Sm_2Co_{17} sample proved to be the most resistant to radiation, losing less than one percent of its original magnetic remanence. Sm_2Co_{17} was found to be 10 times less sensitive to proton radiation compared to $SmCo_5$, consistent with data measured at CERN. The Nd-Fe-B samples proved to be extremely sensitive to ionizing radiation, losing essentially all of its magnetization at a dose of 70 megarads and over 50 percent loss at four megarads, more than five order of magnitudes more sensitive than Sm_2Co_{17} [Ref. 5: pp. 1-3]. Thermal effect studies were conducted using the same techniques utilized at CERN, except that the samples were heated to a temperature of 250 °C. The Hicorex 90B suffered the greatest magnetization loss from thermal effects, a two percent drop in remanence. The maximum temperature reached during radiation was 125 °C for a period of 30-75 hours. Therefore, temperature was not considered the major factor in remanence loss [Ref. 5: pp. 1-4].

In 1986, LANL conducted a further study of radiation effects on Nd-Fe-B and Sm-Co magnets at the Omega West Reactor Site. Gamma radiation effects were also studied on two different samples of Nd-Fe-B using a Co^{60} source. However, the Nd-Fe-B samples that were irradiated by gammas to a total dose of 49 megarads exhibited no

decrease in remanence loss. [Ref. 6: p. 3]. This result coupled with the proton irradiation measurement from TRIUMPF, suggest that for Nd-Fe-B, the loss of remanence is not strictly a total dose effect, but radiation mechanism dependent as well. Nd-Fe-B sample proved much more sensitive than the Sm_2Co_{17}, which is consistent with previous experiments. Also, three different manufactured Nd-Fe-B samples were irradiated at LANL reactor site with equivalent maximum neutron fluence. Each sample measured a different amount of remanence loss, which suggest that radiation effects is also dependent on the microstructure and manufacturing techniques of the magnetic alloy. Table 1 on page 8 summarizes the results from the previous experiments just mentioned.

The radiation runs scheduled at LLNL's Linac were directed primarily to continue research in gamma radiation effects on Sm-Co and Nd-Fe-B permanent magnets. The prior studies established the effects neutron and proton radiation have on these magnets. Aside from Co^{60} gamma radiation conducted at Los Alamos, experimental results were essentially non-existent. Therefore, a team at LLNL, headed by Dr. Nicholas Colella and Dr. Bernhard Kulke, scheduled radiation runs to continue an in-depth study to examine the responses of permanent magnets used in FELs due to radiation damage exposure and consequenct damage. The following is a list of magnetic characteristics [Ref. 3: pp. 1-2]:

1. Halbach hybrid wigglers require REPMs to operate near their coercivity points and to possess nearly linear B-H curves in proximity to ther coercivity points. Non-linearities introduced into the B-H curve by radiation damage can profoundly degrade the performance of a wiggler.

2. A high degree of cancellation of field errors demands that magnets be tightly matched in remanence. Further dispersion of remanence caused by radiation damage will degrade the initial matching. Hence, variances in remanence of a collection of magnets must be determined based on post irradiation results.

3. The radiation fields employed in previous studies are not representative of the mixed fields possible in high powered FELs. Electrons lost from a primary beam due to accidental beam spillage, poor emittance, or improper matching, will interact with the beam pipe to produce bremsstrahlung photons, a fission-like spectrum (sub MeV to several MeV) of neutrons and a broad distribution in energy of electrons (deltas and multiple scattered primaries). Thus, in addition to

microstructural damage caused by scattered neutrons and ionization caused by neutrons and electrons, REPMs in high powered FELs can suffer total dose damage from bremsstrahlung photons as well.

4. The creation of an alloy with high coercivity is often described as an "Edisonian" process [Ref. 7: p. 6]. The elemental composition, particle size and details of manufacturing a standard REPM, Sm_2Co_{17} for example, vary widely in industry. Thus, one must exercise caution when using the results from one commercial alloy to predict the behavior of another in an FEL application.

The studies at LLNL are considered extensions of the experiments conducted at LANL, CERN and TRIUMPF and were performed to provide input to the selection of magnetic alloys for future high-powered FELs. The following chapter gives a detailed account of the irradiation runs at LLNL's 100 MeV Linac.

Table 1. SUMMARY OF PRIOR STUDIES

Sample	Alloy	Type of Irradiation	Maximum Dose (x 10^9 rads)	Remanence loss (%)
CERN, 1983: [Ref. 4]				
RECOMA 20	$RECo_5$	proton	9.700	42.70
VACOMAX 200	$SmCo_5$	proton	10.400	106.10
KOERMAX 160	$SmCo_5$	proton	11.400	24.20
KRUPP WIDIA	Sm_2Co_{17}	proton	10.500	2.60
TRIUMPF, 1985: [Ref. 5]				
HICOREX 90B	$SmCo_5$	proton	3.02	13.50
HICOREX 96B	$(SmPr)Co_5$	proton	1.53	6.50
CRUCORE 18	$SmCo_5$	proton	5.81	1.64
CRUCORE 26	Sm_2Co_{17}	proton	5.94	0.30
NeIGT 27	$Nd_2Fe_{14}B$	proton	0.003	55.40
LANL, 1986 (Cobalt 60 Source): [Ref. 6]				
CRUMAX 282	$Nd_2Fe_{14}B$	gamma	48.8 MRads	0.00
NeIGT 27	$Nd_2Fe_{14}B$	gamma	48.8 MRads	0.00

Sample	Alloy	Type of Irradiation	Maximum Fluence (x 10^{18} n/cm²)	Remanence loss (%)
LANL, 1982 (LAMPF): [Ref. 2]				
HICOREX 90B	$SmCo_5$	neutron	1.10	1.88
HICOREX 96B	$(SmPr)Co_5$	neutron	1.20	2.21
LANL, 1986 (Omega West Reactor Site): [Ref. 6]				
CRUMAX 282	$Nd_2Fe_{14}B$	neutron	2.50	79.10
NeIGT 27H	$Nd_2Fe_{14}B$	neutron	2.50	86.80
HICOREX 94B	$Nd_2Fe_{14}B$	neutron	3.80	14.00
INCOR 18	Sm_2Co_{17}	neutron	2.60	0.00
INCOR 22HE	Sm_2Co_{17}	neutron	2.60	0.20

III. EXPERIMENT

As mentioned in the previous section, studies on radiation effects on permanent magnets have focused primarily on effects due to proton and neutron irradiations. Since only few experiments existed concerning gamma radiation effects on REPMs, irradiation runs were scheduled to expose REPMs to high dosage levels of gamma radiation.

A. PRELIMINARY CALIBRATION MEASUREMENTS

Several gamma production targets were available at LLNL's Linac. The target chosen was a composite material known as "heavimet." This material is composed of four percent copper, seven percent nickel and 89 percent tungsten and has a density of 17.1 gr cm³. Since tungsten is the dominant material in this foil, the production target will be occasionally referred to as a tungsten target. Figure 2 on page 10 is a cross sectional view of the target. The production target is composed of the tungsten foil which is attached to a copper layer that forms the lining of the water-cooled support structure. Hitting the production target with an 85 MeV electron beam provided a source of gamma radiation. The irradiation runs were conducted in January and February, 1988.

Prior to the scheduled irradiation runs, preliminary bremsstrahlung dose measurements were made to determine the radiation dosage pattern from the beam center to a radius of 10 cm. This geometry was chosen to accomodate the magnet sample-holder used in the experiment. LiF TLD chips were positioned 38.1 cm from the production target to measure the dose. The beam energy used for the calibration run was 79 MeV. The measured radiation dosage pattern, shown in Figure 3 on page 11[Ref. 8: p. 1], was scaled to 85 MeV and 78.7 cm to correspond to the actual experimental parameters. Geometrically, the resultant pattern width was scaled as R and the dose was scaled as $1/R^2$. The measured on-axis dose was scaled as $(MeV)^{2.5}$, a conversion scaling factor derived from a flash x-ray calculation. An on-axis dose rate of 0.201 gigarads per coulomb of primary electron beam charge was calculated. [Ref. 9: p. 3]

One of the primary concerns of the Linac operator was ensuring that the beam was focused to a size small enough to ensure complete capture by the tungsten disc. To detect whether the beam diameter was within the disc, glass plates were exposed at the TLD chip location to obtain a continuous intensity profile. If a halo effect (beam diameter greater than the tungsten disc) was present, the glass darkened due to its

9
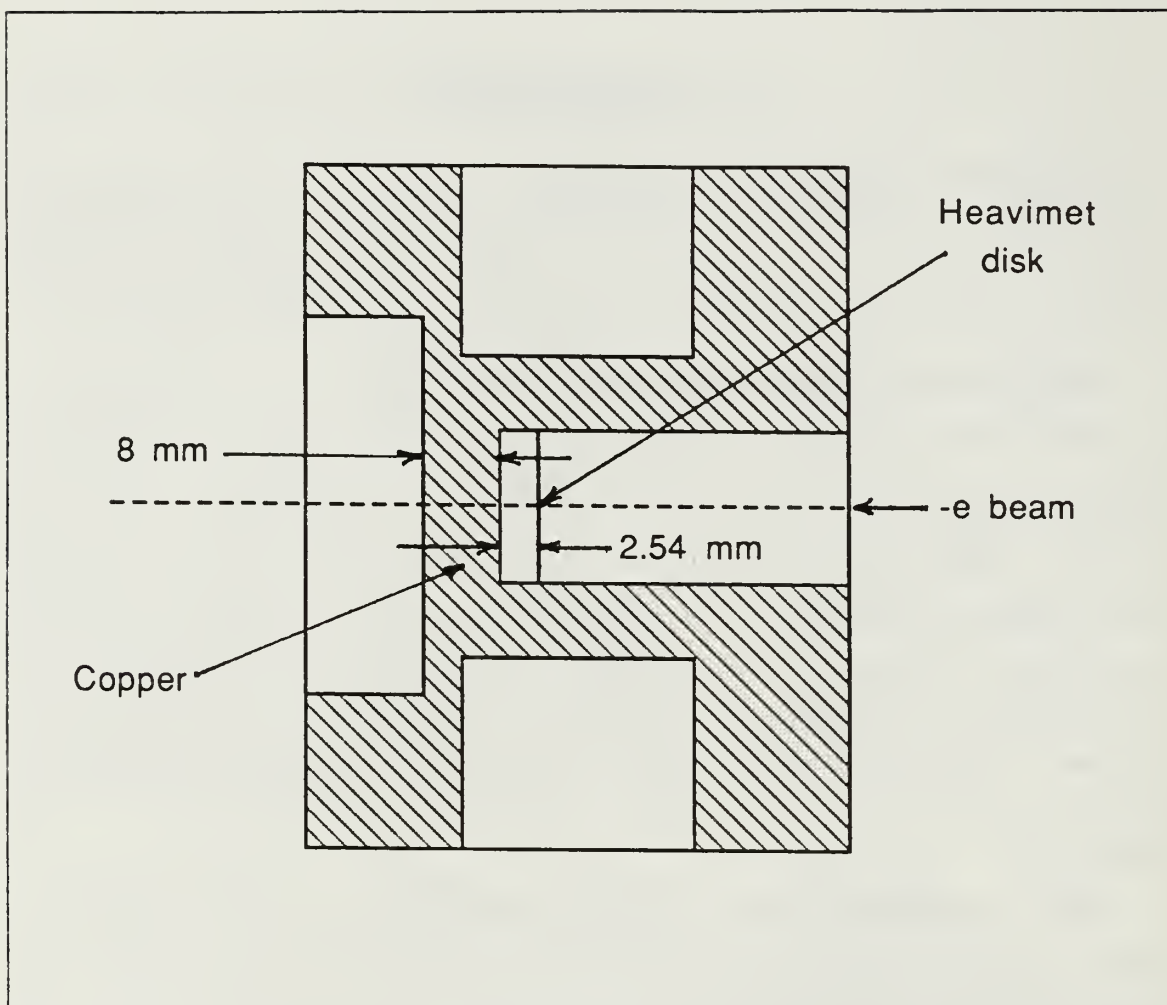
Figure 2. Longitudinal Cross Section of the Production Target: where the heavimet disc has radius of 0.94 cm and the copper support structure has a radius of 3.94 cm.

exposure to beam electrons. The radiation dosage pattern in Figure 3 was calibrated assuming that no halo effect existed. The beam radius was estimated at 0.75 cm. [Ref. 8: p. 1]

Prior to the irradiation, LiF TLD chips were used to verify the gamma dose calibration measurements taken in April, 1987. An array of TLDs were positioned 167.8 cm from the production target. The dosimeters were placed at the corners and behind a 10 cm lucite block. The center of the block was positioned on the beam axis. A total charge of 11 microcoulombs were deposited. The dosimeters measured 22 ±5 megarads per coulomb. The pre-calibrated dosage pattern should have given a rescaled dose of
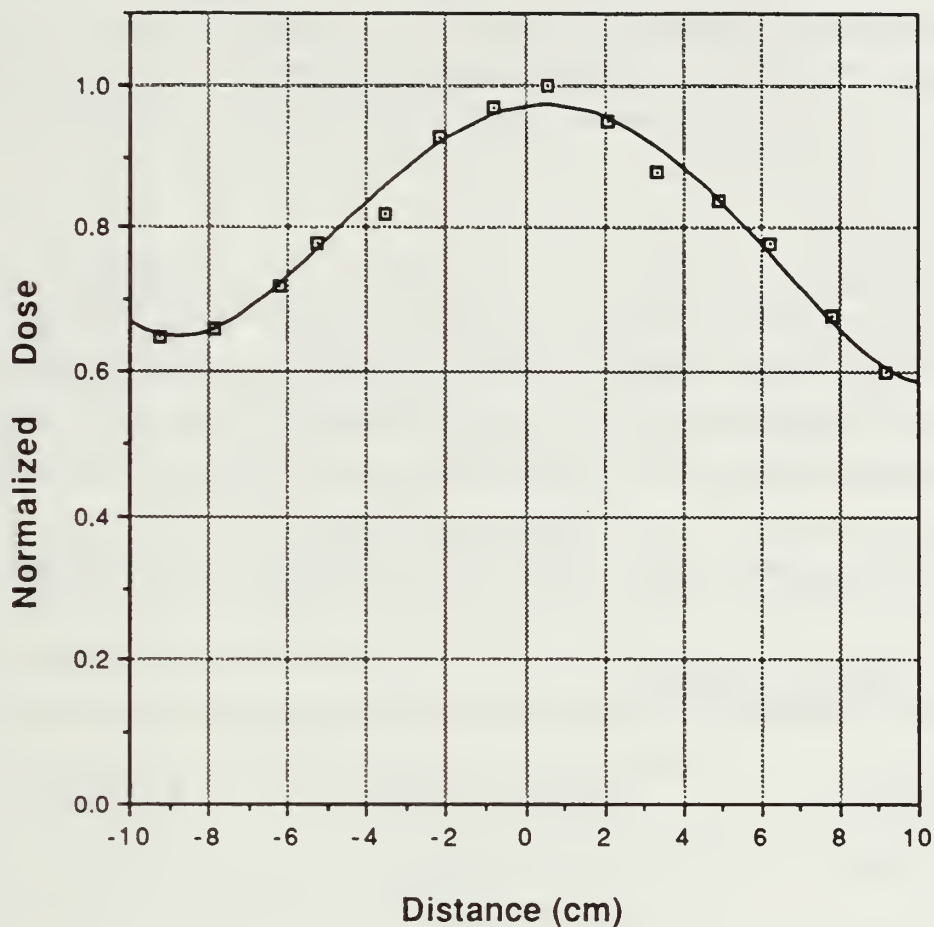
Figure 3.   Normalized Radiation Pattern of Production Target

37 ±15 megarad per coulomb. The disparity could have been generated from the conversion factor derived from the flash x-ray scaling. Keep in mind the large uncertainties produced from the flash x-ray conversion factor [Ref. 9: p. 8]. These parameters were modeled into ITS CYLTRAN to compare its accuracy with the dosimeter readings. ITS CYLTRAN results are in agreement with the TLD measurements as discussed in the following chapter.

CR-39 (LiF) neutron dosimeters were taped to the magnet sample-holder to measure the neutron dose prior to the scheduled irradiation periods. This yielded an average measured dose of 0.5 ±0.3 megarads per coulomb in the sample plane [Ref. 9: p. 3]. A neutron dosimeter was also used to measure the neutron dose at the reference magnet

position. According to its reading of 0.15 megarads per coulomb, the reference magnet, which had been mounted for the duration of the entire experiment on the same plane as the sample wheel holder but shielded from the bremsstrahlung radiation cone by 5 cm thick lead bricks, received a total neutron dose of 3.7 megarads, significantly less than gamma radiation exposure.

B. EQUIPMENT

The experiment conducted at LLNL exposed a total of 21 permanent magnets. Samples from four different manufacturers were irradiated. Table 2 lists the types of rare earth magnets used. Each sample had a cylindrical shape measuring 8 mm in diameter and 12 mm in length. The samples were mounted on the spokes of a water-cooled aluminum wheel pictured in Figure 4 on page 14. This sample wheel holder was part of a fully automated "in-situ magnetometer" apparatus shown in Figure 5 on page 15 which was designed to remotely measure the remanence of each sample [Ref. 3: p. 3].

Table 2. REPM SAMPLES

ALLOY	MANUFACTURER	B_o (kilogauss)
$Nd_2Fe_{14}B$	Crucible Materials	4.85
$Nd_2Fe_{14}B$	Hitachi Magnetics	4.78
Sm_2Co_{17}	Shin-etsu	4.35
$Pr_{15}Fe_{79}B_6$	Advanced Material Corp	4.58

The magnetometer was designed to hold eight samples, but during the irradiation runs, only six holders were used. The reason for this was to achieve a significant dosage differential between the inner and outer three magnets. The two spokes with single sample holders did not provide adequate distance between the other magnets and therefore were not used. Each sample was water-cooled to eliminate thermal effects. The temperature of each sample was monitored with resistive temperature detectors (RTD's). Temperature and remanence measurements were interrogated periodically with a computer interfaced with the in-situ magnetometer apparatus. This was made possible by two

pneumatic cylinders, controlled by relays and a stepping motor. See Figure 5 for the location of these control devices. A servo motor was designed to drive the coil platter. The coil platter (a lucite wheel resembling a film reel) moved between three discrete radii on the sample wheel platter by the pneumatic cylinders or positioners. The positioners were controlled by the computer. The sample platter was designed to rotate $\pm 90°$ with the stepper motor. The individual samples were brought into a position where they could be interrogated by a pair of search coils (rotating coils) on the coil platter. The platter rotated freely (slowly) when the magnets were being irradiated. When magnets were being interrogated, the beam was secured off and the wheel rotation rate was increased to 785 RPMs. The induced signals were brought out through low-noise, mercury slip rings to a gated integrator, digitized and recorded on computer disk. [Ref. 10: p. 2]

A calibration to determine the accuracy of the in-situ apparatus measurement was performed with a set of samples that had been magnetized to different levels and measured with the integrating fluxmeter. The calibration curve is shown in Figure 6 on page 16. The one to two percent errors are due to small differences in the position of the same magnet with respect to the search coil pair. For each magnet sample, the repeatability between successive measurements was also on the order of one to two percent. The remaining error could be due to dynamic misalignments between the vibrating sampling wheel and the magnet samples.

The charge deposited on the production target was measured directly with an Ortec Model 439 digital current integrator interfaced to an Ortec scalar to provide charge in coulombs. A conversion factor was applied based on the ratio of the average current measured at the production target to the average current measured at the beam dump without the production target, because the production target was less than range thick. [Ref. 9: p. 2]

The open circuit remanence of each sample before and after irradiation was measured using an integrating fluxmeter (Walker Scientific Model MF-3D). [Ref. 9: p. 1]

C. IRRADIATION RUNS

1. Cobalt 60 Source

Two samples of Sm-Co alloy were placed in a Co^{60} tank to accumulate gamma radiation. The samples were Shin-etsu R26H (Sm_2Co_{17}) and Vacomax 225 ($SmCo_5$). Both samples were exposed to a total dose of 1.4 gigarads. Initial and post irradiation
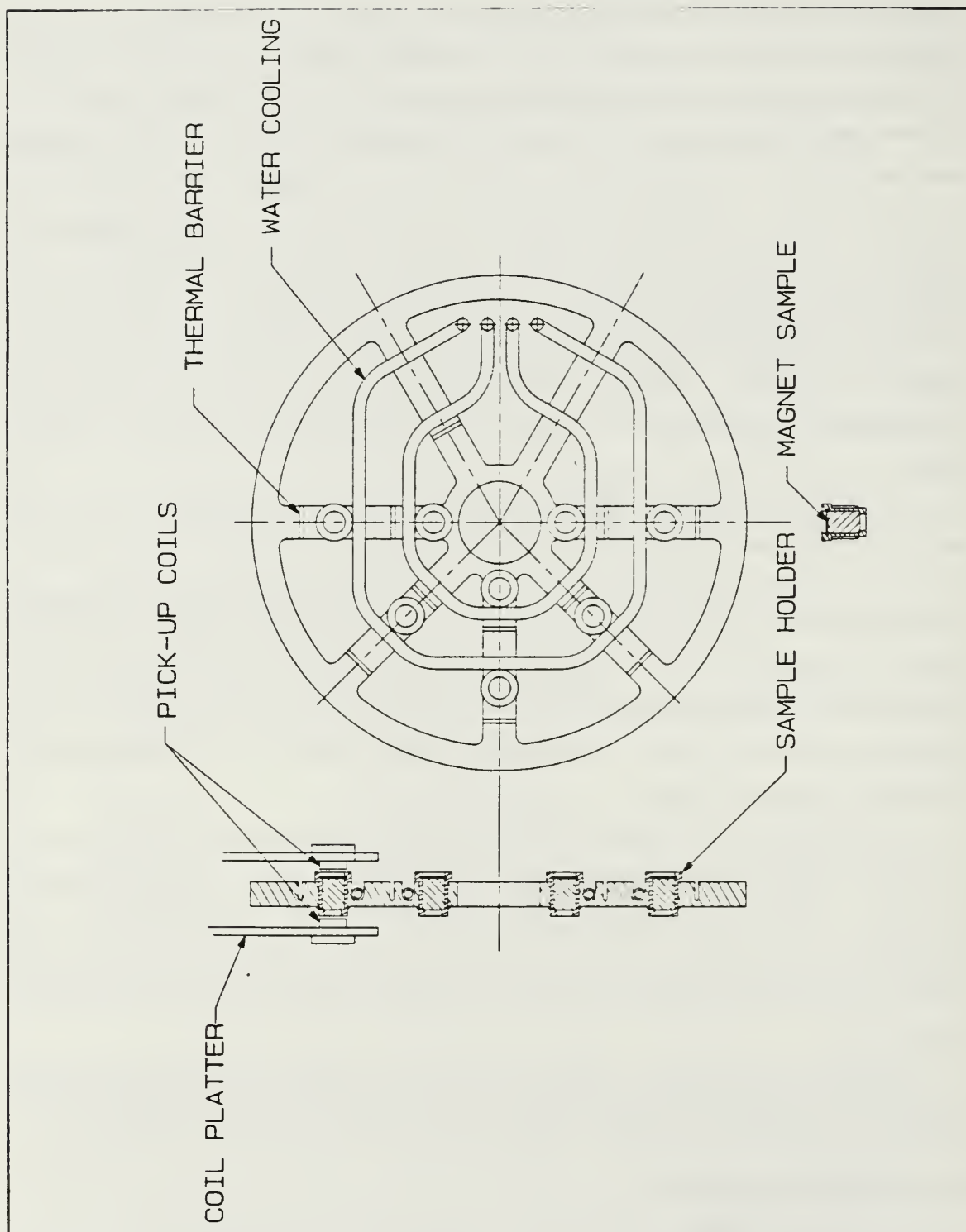
Figure 4.   Aluminum Sample Wheel Holder

14

REVOLVING COIL

COIL PLATTER

SAMPLE PLATTER

REFERENCE MAGNET

GUIDE WHEELS

COIL DRIVE

ADJUSTABLE MAGNETOMETER
ASSEMBLY

SAMPLE PLATTER
DRIVE

PNEUMATIC CYLINDERS
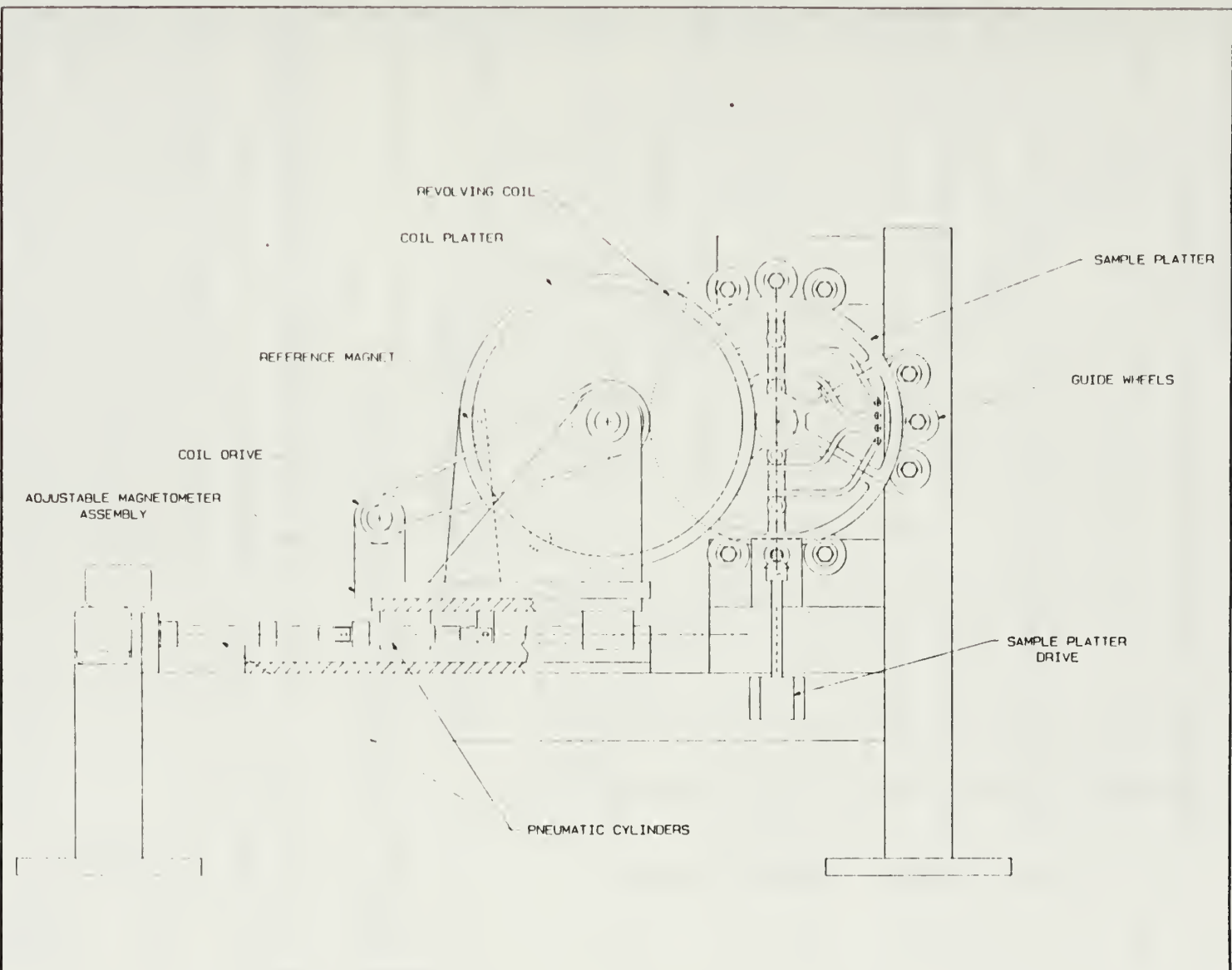
Figure 5. In-Situ Magnetometer Apparatus

15
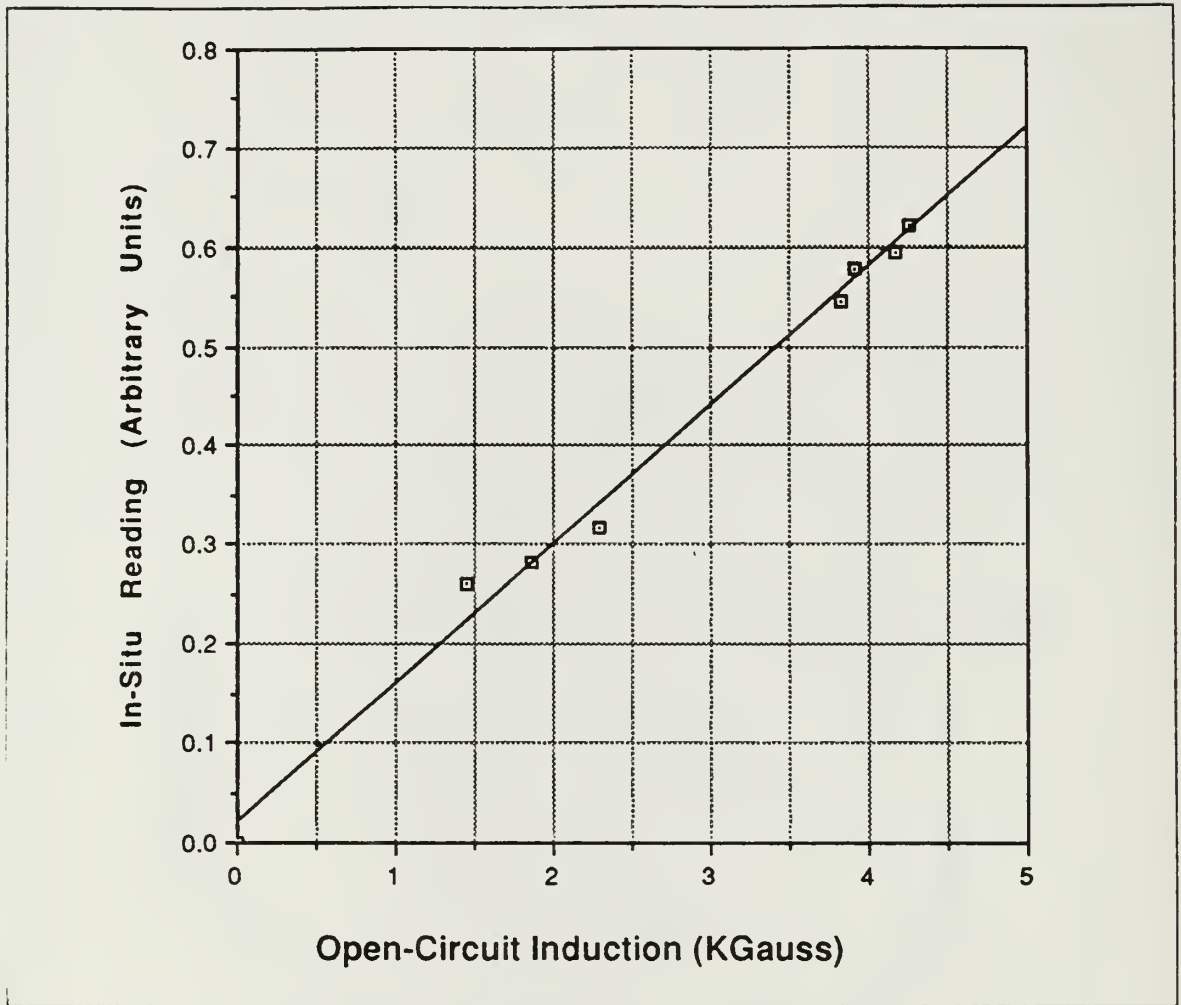
Figure 6.   Calibration of the In-Situ Magnetometer

remanence readings were measured by a Hall probe gaussmeter.   Both samples experienced no experimentally resolvable remanence loss.

One sample of Nd-Fe-B alloy (Crumax 355) was exposed to a total dose of 69 megarads by the Co^{60} source.   No remanence loss was detected in this sample as well.

The uncertainties in measuring the remanence of each sample are due to the Hall probe gaussmeter sensor being comparable in size to the diameter of the magnets. Therefore, the measurement is very dependent upon the exact positioning of the probe relative to the magnet.   Also, the measurement was observed to vary with temperature.

2. Direct Electron Beam

Two magnet samples were irradiated with a direct 82 MeV electron beam. The samples tested were Vacomax 225 (SmCo$_5$) and Crumax 355 (Nd$_2$Fe$_{14}$B). The beam parameters used were set at an average current of 600 microamps using pulses of 2.8 microsecond duration. A total of 25 pulses were deposited on the magnet samples for an estimated total dose of 36 kilorads. The Vacomax 225 measured no remanence loss whereas the Crumax 355 sample measured a loss of 1.5 percent in remanence field, which was a statistically significant drop. This seems to suggest that a direct high energy electron beam causes more remanence loss than Co^{60} gamma fields for the same total dose.

The purpose of these measurements was to determine how much beam current would be required to induce a measurable loss in remanence for each magnet. This in turn would establish an estimated interrogation time interval for the irradiation runs utilizing the in-situ magnetometer apparatus.

3. Bremsstrahlung Radiation

An 85 MeV electron energy beam was used for all irradiation runs. Beam and other pertinent parameters are listed in Table 3 for the two scheduled periods.

Table 3. LINAC OPERATING PARAMETERS

	26 JAN 88	16-19 FEB 88
Distance from target (cm):	49.2	78.7
Measured current at production target (μamps):	28.0	70.0
Measured current at beam stop (μamps):	60.0	155.0
Production target/beam stop current ratio:	2.14	2.21
Pulse repetition rate (Hz):	60.0	120.0
Estimated beam spot diameter (cm):	1.0	1.0

Six samples of Hicorex 94EB (Nd$_2$Fe$_{14}$B) were irradiated during run 1. (Refer to Table 4 on page 18 for a description of each irradiation run). An estimated total dose

of 0.4 gigarads was deposited on the magnet sample that was positioned on the beam axis. Post irradiation measurements on the integrating fluxmeter recorded a three to five percent drop in remanence. [Ref. 9: p. 4]

Table 4. SUMMARY OF THE IRRADIATION RUNS

Run Nr	Date	Samples	Time Exposed (hours)	Charge (coul)	Number Irradiated
1	26 Jan 88	Hicorex 94EB	3.0	2.0	6
2	16/17 Feb 88	Crumax 355	8.0	4.6	6
3	18 FEB 88	Shin-etsu R26H	7.0	3.9	4
		AMC	7.0	3.9	2
4	19 Feb 88	Hicorex 94EB	8.0	5.9	2
		AMC	8.0	5.9	1
5	18/19 Feb 88	Shin-etsu R26H	15.0	8.9	2
		AMC	15.0	8.9	1

Six samples of Crumax 355 ($Nd_2Fe_{14}B$) were irradiated during run 2. When measurements on these samples were recorded on the second day, the interrogation readings measured zero remanence due to mechanical failure of the in-situ magnetometer. On the following morning, we discovered the lucite wheel containing the search coils cracked due to radiation damage. The damaged wheel caused erroneous zero remanence measurements. After measuring the post irradiation remanence of these samples on the integrating fluxmeter, only a two percent loss was measured. A calculated dose of 0.92 gigarads was deposited [Ref. 9: p. 4].

During run 3, the six Crumax 355 samples were replaced by four samples of Shin-etsu R26H (Sm_2Co_{17}) and two samples of AMC ($Pr_{15}Fe_{79}B_6$). These samples were

irradiated for a total of seven hours. Active cooling of the samples was no longer feasible since the water circulation system also suffered radiation damage.

Two Shin-etsu R26H samples and one of the AMC samples were replaced with two samples of Hicorex 94EB and a different sample of AMC during runs 4 and 5. The remaining two samples of Shin-etsu R26H and the other AMC sample remained in their respective positions to accumulate more dose. The two Shin-etsu R26H and the AMC samples that were irradiated for two days (15 hours) received a total dose of 1.5 and 1.8 gigarads respectively. Post irradiation measurements on the integrating fluxmeter measured no loss in remanence for the Shin-etsu R26H sample. The AMC samples received the highest dose total and recorded the biggest drop, a 75 percent loss in remanence. [Ref. 9: p. 5]

D. TEMPERATURE EFFECTS

For the first three scheduled days of irradiation runs, the temperature of each sample was monitored. Temperature recorded for each sample was maintained at around room temperature. Therefore, remanence loss for the Hicorex 94EB and Crumax 355 samples were not due to temperature. For the irradiation runs conducted on February 18 and 19, the water cooling system was not available and temperature was not monitored. The reference magnet was not water-cooled during the entire irradiation period. When the in-situ magnetometer apparatus was operational, an average temperature of 26 °C was measured after four hours of irradiation. Based on this information, an estimated temperature for the samples irradiated on February 18 and 19, after the apparatus was damaged, reached a temperature slightly higher than 26 °C, since total irradiation time was greater, eight hours, and the magnet samples were exposed directly to the bremsstrahlung radiation. The temperature still was maintained well below the stabilizing temperature of each magnet sample. Therefore, temperature had minimal effect throughout the entire experiment.

E. RESULTS

Table 5 on page 20 summarizes the irradiation results. Crumax 355 ($Nd_2Fe_{14}B$) was irradiated using a direct electron beam. A loss in remanence was measured which could have been due to the positioning error of the hall probe. The values for the normalized remanence at maximum dosage for the samples exposed to bremsstrahlung radiation were computed using the following linear fit equations used to plot the curves in Figure 7 on page 21:

$$B_r/B_o = 1.0 + ax$$

where a = -0.14 for Hicorex 94EB, -1.24 x 10^{-2} for Crumax 355, 2.25 x 10^{-5} for Shin-etsu R26H and -0.33 for AMC.

Table 5. **RESULTS OF IONIZING RADIATION ON REPM SAMPLES:** Values for bremsstrahlung radiation corresponds to the fit values from Figure 7 on page 21.

Sample	Alloy	Temp (°C)	Maximum Dose (10^9 rads)	Normalized Remanence at Max Dose
Cobalt 60 Source:				
VACOMAX 225	$SmCo_5$	24	1.400	1.000
SHIN-ETSU R26H	Sm_2Co_{17}	24	1.400	1.000
CRUMAX 355	$Nd_2Fe_{14}B$	24	.069	1.000
Direct Electron Beam:				
VACOMAX 225	Sm_2Co_{17}	nm	36.0krads	1.000
CRUMAX 355	$Nd_2Fe_{14}B$	nm	36.0krads	.985
Bremsstrahlung Radiation:				
HICOREX 94EB	$Nd_2Fe_{14}B$	24	.396	.945
CRUMAX 355	$Nd_2Fe_{14}B$	23	.918	.989
SHIN-ETSU R26H	Sm_2Co_{17}	28	1.515	1.000
AMC	$Pr_{15}Fe_{79}B_6$	28	1.782	.412

nm - not measured

Post irradiation remanence was measured on an integrating fluxmeter and normalized. ITS/CLYTRAN simulation codes were used to plot the normalized remanence
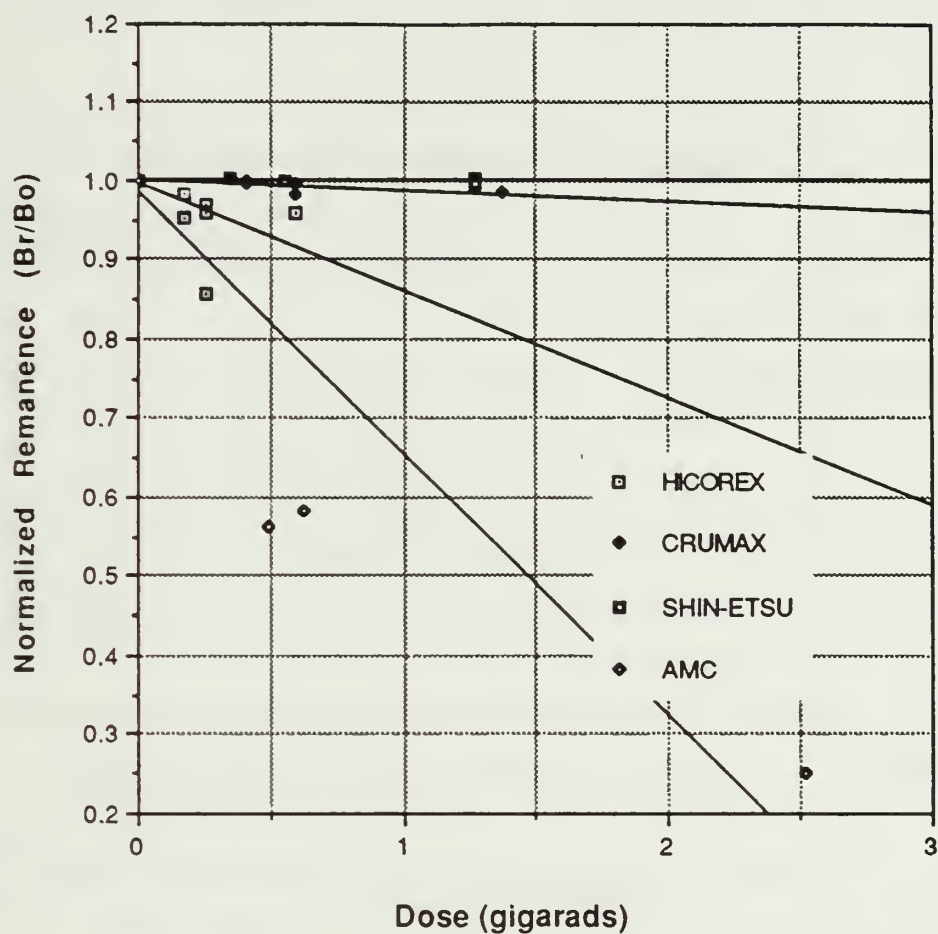
Figure 7. ITS/CYLTRAN Plot of Normalized Remanence vs Dose

versus dose in gigarads for each magnet alloy. Energy deposition in gigarads per coulomb was computed using CYLTRAN and converted to gigarads based on the total charge deposited on each magnet sample recorded during the irradiation runs. A linear fit as previously described was used to plot the curves for each magnet sample.

The same procedure was used to plot the results obtained from the irradiation runs. The difference between the two plots was that the total dose computed was based on the flash x-ray calculation described in the Preliminary Calibration Measurements section of this chapter. Figure 8 on page 23 represents the plot which lays out the general trend

of remanence loss for each magnet sample irradiated and dose calculated using the flash x-ray scaling. A linear fit was also used to plot the curves for each magnet sample with the exception of the AMC sample. Refer to Appendix C for a description on how ITS/CYLTRAN codes are used and executed.

Figure 8, which is the plot produced from the flash x-ray calculation is very similar to Figure 7, the plot produced from the ITS/CYLTRAN simulation. The only significant difference that exist is the nonlinear curve for the AMC sample shown in Figure 8. The disparity could have been attributed to the uncertainties in the flash x-ray calculation used to compute the total dose.

In general, ITS/CYLTRAN computed higher on-axis dose for each magnet alloy compared with the data obtained from the flash x-ray calculation. ITS/CYLTRAN, however, computed a slightly less dose for those magnets positioned on the outer radius of the magnet sample holder. (See Figure 9 on page 24 for the magnet positions on the sample holder). Table 6 on page 26 shows the difference in dosage values computed by ITS/CYLTRAN and the flash x-ray scaling used at LLNL for the different magnet samples positioned on the sample holder.

For the samples that suffered noticeable demagnetization, a change in the coercivity field might occur. This can be examined by plotting a demagnetization curve in a hysteresis graph. Future studies in terms of the Barkhausen effect [Ref. 11: p. 46], which is an experimental characterization of the dynamics of domain wall movement, precludes demagnetizing the irradiated magnets to obtain the hysteresis loop required to determine the coercive force of the sample. Studies of the Barkhausen effect on the irradiated samples are planned for June and July, 1988 to investigate the causes to why radiation exposure reduces the remanence in permanent magnets. [Ref. 9: p. 3]

A Crumax 355 (Nd-Fe-B alloy) was used and positioned along the same plane with the sample-holder. This reference magnet was shielded from the bremsstrahlung cone, but still received one-third to one-half the neutron dose of the other samples since neutron radiation is not as directional. Exposure to neutron dose was the only means of remanence loss in which the reference magnet could have encountered, since the reference magnet was shielded from bremsstrahlung radiation. Since post irradiation measurements recorded no remanence loss, we can conclude that neutron fluence had no significant effect on remanence loss on the magnet samples irradiated based on the dosimeter measurements taken prior to irradiation. [Ref. 9: p. 6]
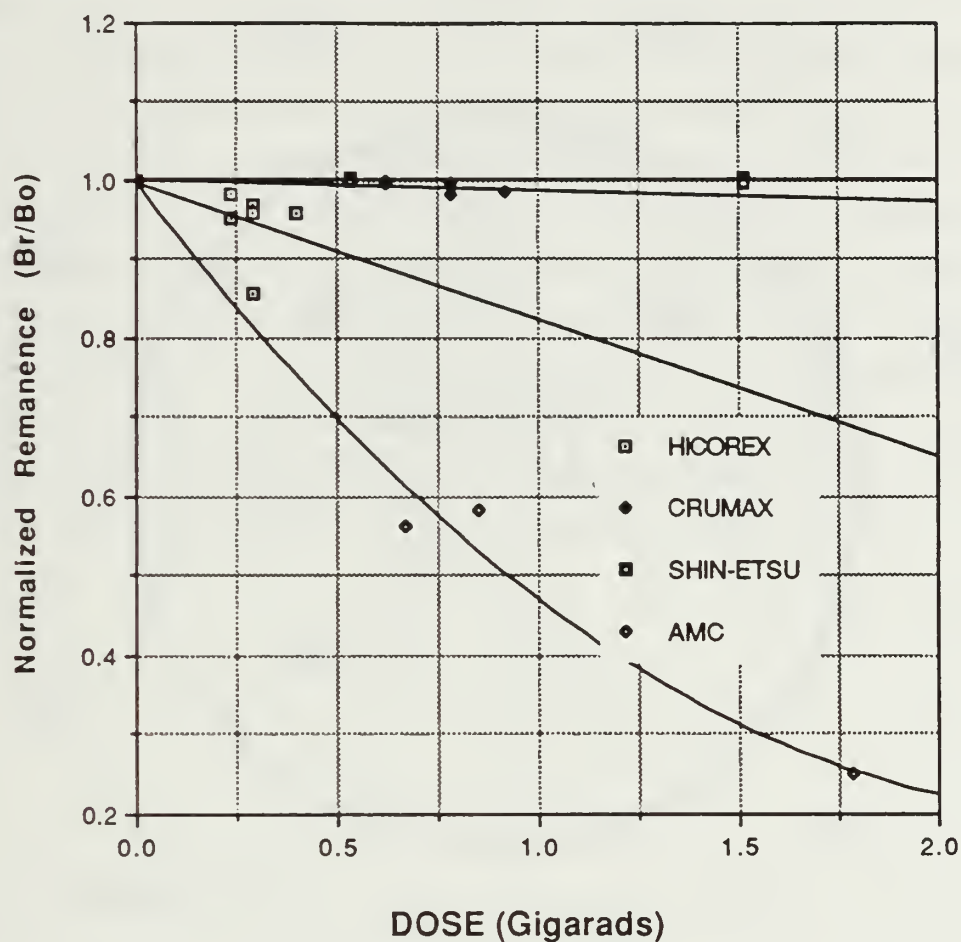
Figure 8.   Flash X-ray Scaling Plot of Normalized Remanence vs Dose

F. CONCLUSIONS

In conclusion, the experimental results show that the Shin-etsu R26H (Sm_2Co_{17}) magnets are the most radiation resistant of the materials studied. Sm_2Co_{17} provides the greatest hardness against bremsstrahlung irradiation. ITS CYLTRAN analysis in the next section will show that gamma radiation is the dominant field produced from the production target.

Comparing the results of the two $Nd_2Fe_{14}B$ alloys, Crumax 355 and Hicorex 94EB, Hicorex 94EB proved to be less resistant. The magnets were manufactured by different

23
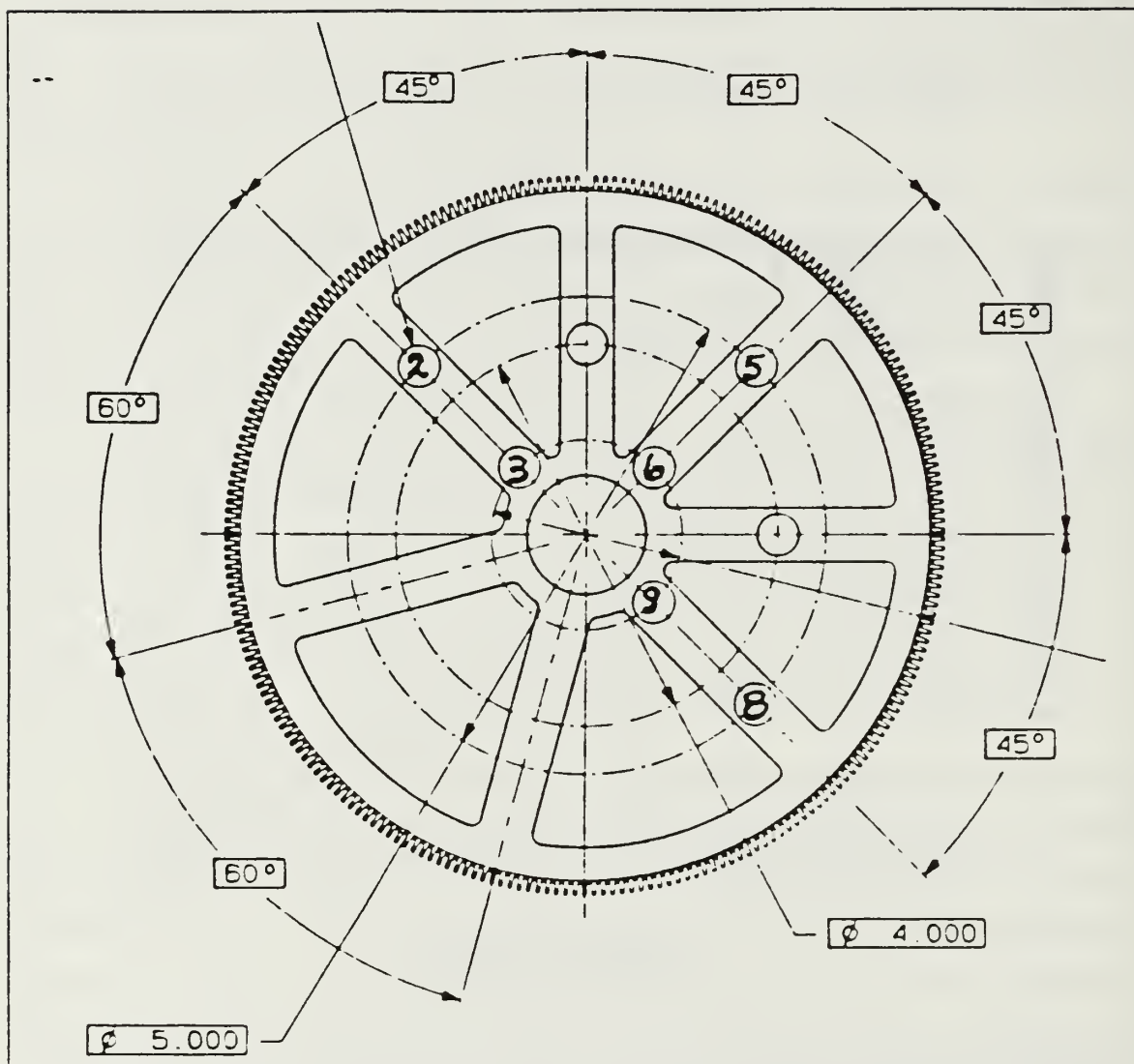
Figure 9. Magnet Positions on the Sample Wheel Holder: where the radius of the inner magnets is 2.54 cm and the outer magnet is 6.35 cm.

companies, which confirms that manufacturing techniques of similar alloys have impact on radiation hardness. Barkhausen effect studies may provide added insight to these differences.

Based on the neutron dosimeter readings placed at each sample site, including the reference magnet, remanence loss due to neutron exposure was insignificant.

The temperature effect on permanent magnets was held minimal to none, since the Curie temperature for each magnet alloy is far above its operating temperature during

radiation exposure. The Curie temperatures for iron and cobalt are 770 °C and 1131 °C respectively.

During the planning phase, prior to the irradiation runs, numerous test and equipment (i.e. in-situ magnetometer interfaced with computer system) calibrations were made to ensure accurate data would be recorded throughout the experiment. We continued the experiment in spite of equipment failure and key results and conclusions were obtained during these final days of scheduled irradiation runs. Our results indicate that to acquire the gross radiation effect measurements, the sophisticated apparatus used was not needed. However, it would be most useful in studies where prototype magnets of different compositions are simultaneously exposed. This would allow us to mix different magnet samples on the same wheel and expose them to the same radiation environment and trace their demagnetization curves out to significant remanence losses.

Table 6. COMPARISON BETWEEN ITS/CYLTRAN AND FLASH X-RAY SCALING

DATE	MAGNET TYPE	CHARGE (COUL)	MAGNET POSITIONS					
			2	5	3	6	9	8
====	====== ====	===== ======	===	===	===	===	===	===
28JAN88	HICOREX 94EB	1.968						
	NORMALIZED REMANENCE:		.983	.969	.958	.961	.857	.952
	FLASH X-RAY SCALING (GIGARADS):		.237	.289	.289	.396	.289	.237
	ITS DOSE (GIGARADS):		.177	.258	.258	.590	.258	.177
17FEB88	CRUMAX 355	4.568						
	NORMALIZED REMANENCE:		1.000	.996	.982	.986	.983	.997
	FLASH X-RAY SCALING (GIGARADS):		.624	.781	.781	.918	.781	.624
	ITS DOSE (GIGARADS):		.411	.598	.598	1.369	.598	.411
18FEB88	SHIN-ETSU	3.896						
	NORMALIZED REMANENCE:		1.002				1.000	
	FLASH X-RAY SCALING (GIGARADS):		.533	.667	.667	.783	.667	.533
	ITS DOSE (GIGARADS):		.348	.558	.558	1.369	.558	.348
18FEB88	AMC	3.896						
	NORMALIZED REMANENCE:			.563				
	FLASH X-RAY SCALING (GIGARADS):		.533	.667	.667	.783	.667	.533
	ITS DOSE (GIGARADS):		.392	.493	.493	1.108	.493	.392
19FEB88	SHIN-ETSU	8.866						
	NORMALIZED REMANENCE:			1.005			.995	
	FLASH X-RAY SCALING (GIGARADS):		1.212	1.515	1.515	1.782	1.515	1.212
	ITS DOSE (GIGARADS):		.792	1.270	1.270	2.747	1.270	.792
19FEB88	AMC	8.866						
	NORMALIZED REMANENCE:					.250		
	FLASH X-RAY SCALING (GIGARADS):		1.212	1.515	1.515	1.782	1.515	1.212
	ITS DOSE (GIGARADS):		.893	1.122	1.122	2.522	1.122	.893
19FEB88	HICOREX 94EB	4.970						
	NORMALIZED REMANENCE:		.961					.945
	FLASH X-RAY SCALING (GIGARADS):		.679	.849	.849	.999	.849	.679
	ITS DOSE (GIGARADS):		.447	.651	.651	1.490	.651	.447
19FEB88	AMC	4.970						
	NORMALIZED REMANENCE:			.582				
	FLASH X-RAY SCALING (GIGARADS):		.679	.849	.849	.999	.849	.679
	ITS DOSE (GIGARADS):		.500	.629	.629	1.414	.629	.500

IV. DOSIMETRY ANALYSIS USING ITS/CYLTRAN

ITS CYLTRAN Monte Carlo simulation codes were used to describe the production and transport of electrons and photons through materials of different materials of cylindrical geometry. These codes were utilized to determine electron and photon energy spectra, angular spectra and resulting energy deposition in materials [Ref. 12: p. 6]. Appendix C describes the use and execution of ITS/CYLTRAN codes.

The experimental configuration at LLNL's 100 MeV Linac was modeled with ITS/CYLTRAN codes to calculate the dose deposited on the three different magnet alloys. A comparison was made between the dose calculated using CYLTRAN and the measured results obtained with dosimeters. The result compare favorably.

A. ENERGY DEPOSITION

CYLTRAN was used to calculate energy deposition on a circular disc one centimeter thick and 10 cm in radius made of a given magnetic material. Sm_2Co_{17}, $Nd_2Fe_{14}B$ and $Pr_{15}Fe_{79}B_6$ were analyzed during different runs. The radius corresponded to the radius of the sample wheel holder used in the experiment. Ten subzones were used to calculate the dose at one centimeter intervals from the center of the disc. This number of subzones allowed the dose to be determined at the corresponding magnet position on the sample holder. (Refer back to Figure 9 on page 24 for the magnet positions on the sample holder).

Angular divergence and beam energy smearing were common operating characteristics of the beam at LLNL's Linac and were modeled into the simulation. Detailed descriptions of angular divergence and beam energy smearing will be given later in this section. An experimentally determined beam radius 0.5 cm was used in all ITS/CYLTRAN simulation runs. Table 7 on page 34 through Table 9 on page 38 give the computed doses of primary electrons, photons and the total energy deposited used to plot the radiation dosage patterns. Figure 10 on page 35 through Figure 12 on page 39 provide the radiation dosage patterns for the magnet samples. (All tables and figures referenced are at the end of this chapter). The total energy deposited in each magnet includes contributions from primary and secondary electrons as well as gamma radiation. The number next to each dose value represents the calculated uncertainty. It represents a measured percentage of the calculated value. ITS calculates the uncertainty

based on stochastic processing as each incident electron traverses a segment of the medium. This process is initiated based on the number of histories and batches simulated.

As shown in Figure 10 on page 35 through Figure 12 on page 39, the shape of the dosage patterns are relatively the same. The slight difference in values can be attributed to the difference in density of each alloy. The measured densities for Sm_2Co_{17}, $Nd_2Fe_{14}B$ and $Pr_{15}Fe_{79}B_6$ are 8.39, 7.60, and 10.20 gr/cm³ respectively. Sm_2Co_{17} and $Pr_{15}Fe_{79}B_6$, which has a higher density, received a slightly higher dose compared with $Nd_2Fe_{14}B$. Notice also that for each alloy, bremsstrahlung radiation is the dominant field. Since tungsten has a high atomic number, the bremsstrahlung radiation is correspondingly high. The fraction of energy loss of primary electrons that are given off as photons are more dominate as electron energy increases. This energy loss by radiation, known as bremsstrahlung, is proportional to Z^2 where Z is the atomic number material and increases linearly with the electron energy. This accounts for the relatively low energy deposited by primary electrons as shown on each graph.

B. DOSAGE DEPOSITION ON VARIOUS MATERIALS

Energy deposition on various materials was modeled using ITS/CYLTRAN to determine how the absorbed dose at the beam axis varies in different materials. The simulated radiation dosage was produced by an 85 MeV electron beam of radius 0.5 cm on a production target similar to the one used at LLNL's Linac. Table 10 on page 40 list the types of materials and alloys used in these simulation runs and compares them with the relative dose to silicon. The comparison with silicon was made because silicon is a common element used in dosimeters to measure radiation effects. Silicon is also the material used in semi-conductors, which is one of the materials of primary interest with respect to radiation hardness. Using the same operating parameters for each material, the absorbed dose deposited on the common material used in dosimetry, Ca, Si and LiF are a factor of three less than those elements and alloys used to manufacture magnets.

C. PRELIMINARY MODELING

Prior to establishing the final model just previously discussed, a series of preliminary runs were conducted to compare the differences between various input parameters. The first comparison made was between the electron energy spectra of tungsten and the composite material "heavimet" (4% Cu, 7% Ni, 89% W). Since the production target used at LLNL's Linac was heavimet, the energy and angular spectra between the heavimet and pure tungsten were generated to determine any differences. Figure 13 on page 41 compares the energy spectra generated through a tungsten disc and heavimet

28

using a point source energy beam at 85MeV. More electrons were transmitted in the lower energy spectrum of the tungsten foil compared to heavimet, leading us to the conclusion that tungsten produces more low energy secondaries. Looking at the opposite end of the spectrum, heavimet allowed a greater number of high energy electrons (primaries). These results were expected based on the density of each target. Heavimet has a density of 17.1 gr/cm³ compared to tungsten at 19.3 gr/cm³. The radiation length of a material depends upon its density (for constant atomic number). Since both materials had the same thickness, and the density of heavimet was slightly less than tungsten, more primary electrons would be transmitted through heavimet.

Another comparison run was made to determine what effects beam radius has on the energy spectrum of the heavimet disc. A point source and a monoenergetic electron beam of radius 0.5 cm were compared. The energy and angular distributions (see Figure 14 on page 42 and Figure 17 on page 45), exhibited no significant differences, which implies that beam spot size has minimal effect on the energy and angular spectra for the electrons and photons. This is obviously true only when the beam radius is less than the radius of the heavimet disc. Later in this section, an analysis of beam spot size will be conducted on the actual production target. A difference in primary electrons and gamma radiation dosage patterns will be observed.

D.   ANGULAR DIVERGENCE

Angular divergence considers the angular distribution of the source particles with respect to the beam axis. The divergence angle was determined by measuring the effective aperture of the quadrupole magnets and the diameter of the production target, as well as the distance between them. An angle of 0.18° was calculated based on these dimensions. Angular divergence was modeled by CYLTRAN. Using a 0.5 cm beam radius and an 85 MeV electron energy beam for the electron source, Figure 18 on page 46 through Figure 21 on page 49 compares the energy and angular energy spectra for transmitted electrons and photons through heavimet for a beam with and without angular divergence. No significant difference was noted which was expected since the divergence angle was significantly small.

E.   ENERGY SMEARING

Energy smearing is defined as the energy distribution describing the electron beam. Energy smearing at LLNL's Linac resembles a Gaussian distribution with a five percent energy drop occurs at the full width half maximum (FWHM) point on the Gaussian distribution curve. A five percent energy smearing was modeled into CYLTRAN to

observe the effects it would have on the energy spectrum for transmitted electrons. Continuing to use a 0.5 cm beam radius and an 85 MeV electron energy beam for the electron source, Figure 22 on page 50 through Figure 25 on page 53 compares the energy and angular spectrums for transmitted electrons and photons through heavimet for a beam with and without energy smearing. The only significant difference noted is the gradual decrease of the number of electrons/MeV at the higher energy bins for the energy distribution modeled with energy smearing. This was expected since the energy at the outer diameter of the electron beam decreases to 79 MeV. Since a noticeable difference occurred, energy smearing was modeled into the remaining CYLTRAN runs.

F. HEAVIMET DISC VS THE PRODUCTION TARGET

A full scale drawing of the longitudinal cross section of the production target used during the irradiation runs is shown in Figure 2 on page 10. The 2.5 mm thick heavimet disc is cooled by an 8 mm thick copper layer support structure. A comparison run was simulated using the heavimet disc with and without the copper layer to determine how the energy and angular spectrums differed for electrons and photons. Angular divergence and energy smearing was included into the modeling. Figure 26 on page 54 compares the energy spectrum for the heavimet disc and the production target with the copper layer. As shown, a significant difference exist at the higher energy bins. A decrease in the number of electrons/MeV occurred when the copper layer was added. This suggest that the combined thickness of the heavimet disc and the copper layer made it more difficult for the high energy primary electrons to be transmitted. The majority of the transmitted electrons were the low energy secondaries. By adding the 8 mm copper layer to the heavimet disc, the number of radiation length of the material was increased by over 40 percent. The electron energy loss due to radiation was calculated for both cases. The calculated electron energy loss for a pure heavimet material was 6.1 MeV compared to 16.4 MeV for the production target [Ref. 13: p. 68]. Refering to Figure 26 on page 54, notice the curve representing the production target loses all its energy at around 69 MeV, and the curve for heavimet loses energy significantly at about 74 MeV. This corresponds almost exactly with our calculations. This gives us confidence in the results generated by ITS/CYLTRAN codes. Figure 27 on page 55 through Figure 29 on page 57 are the remaining comparisons between energy and angular spectrums for electrons and photons. Figure 27 on page 55 and Figure 29 on page 57 compare the angular distributions. Note what happens when the copper support structure is added to the heavimet disc. The half-width angle increases for both electron and photon

angular distributions. This is because the radiation length for copper is almost twice as much as tungsten, 12.86 gr/cm² versus 6.76 gr/cm² respectively, which accounts for the greater angular spread of transmitted photons and electrons. Radiation length is inversely proportional to the deflection angle of transmitted photons and electrons which accounts for the increase in half-width angle.

The half-width angle corresponds to the angle for which the 1/e (.368) of the maximum number of electrons or photons per stere-radian per MeV is at. This value can be utilized to position any equipment, apparatus or any material from the radiation source in order to receive a desired dose. Preliminary modeling using ITS/CYLTRAN can greatly aid an experimental setup to achieve optimum results.

G. HALO EFFECT

The halo effect is when the electron beam cannot be focused to a size smaller than the radius of the heavimet disc. As a result, the beam initially hits the copper support structure before the heavimet foil, producing a halo of electrons. Since the radiation length of copper is greater than tungsten, more electrons will transmit through the copper material. A higher exposed dose of electrons will occur at the outer radius of a sample material. This was evident during one of the preliminary experiments prior to the irradiation runs. Glass plates were known to darken when exposed to high levels of electrons. The electron beam during the preliminary experiments were estimated to be greater than the radius of the heavimet foil, and as a result, darken rings were deposited on the glass plates. An electron beam radius of 1.00 cm was modeled into CYLTRAN to verify the occurence of a high level of electron dose. The radius of the heavimet disc is 0.943 cm, which is less than the radius of the simulated electron beam. A simulated run was executed to measure the dose on a disc platter made of LiF (a common material used in TLD chips to measure gamma dose). The radius of the LiF platter was modeled at 10 cm to correspond with the radius of the sample wheel holder. Figure 30 on page 58 shows the dose pattern for the primary electron, gamma radiation and total energy deposited in gigarads per coulomb. As expected, the primary electrons dominate at the outer radius. Figure 31 on page 59 shows the radiation dosage pattern for an energy beam with radius 0.75 cm. Note that the primary electrons dominate only at the outer perimeter of the LiF platter.

H. EXPERIMENTAL VERIFICATION

The only experimental result which we can use to compare ITS/CYLTRAN with was the dose measurement conducted prior to one of the irradiation runs. An array of

LiF TLD chips were positioned 167.8 cm from the production target. The dosimeters measured 22 ±5 megarads per coulomb along the beam axis. This same arrangement was modeled using the ITS/CYLTRAN simulation codes. A 20.4 megarads per coulomb on axis dose was calculated which concurs with the TLD readings. Figure 32 on page 60 shows the radiation dosage pattern for LiF as it pertains to this configuration. The corresponding dosage pattern values are listed in Table 11 on page 61.

I. DISCUSSION OF ERRORS

The calibration curve shown back in Figure 6 on page 16 was used to measure the accuracy of the in-situ magnetometer apparatus. The curve shown was plotted using a linear fit. The one to two percent error was probably due to small differences in the positioning of the sample magnets with respect to the search coils. A part of the error reflects the 0.4 percent error in maintaining a precise rotation rate for the sampling wheel. The remaining error could be due to dynamic misalignments between the vibrating sampling wheel and the samples. [Ref. 9: p. 2]

The uncertainty in the dosimetry calculations computed by ITS/CYLTRAN runs was approximately 10 percent of the calculated dose. The uncertainty due to the modeling of the dose pattern profile is difficult to quantify. The spread in the data shown back in Figure 7 on page 21 may reflect the overall uncertainty, however, we cannot rule out the sample to sample difference in magnets in general, regardless of the manufacturing techniques and the manufacturer.

J. CONCLUSIONS

ITS/CYLTRAN has proven to be a useful tool in analyzing the energy and angular spectra for varying electron beam parameters. The following conclusions can be made from the series of angular and energy spectrums for the electron and photon plots produced by ITS/CYLTRAN:

Beam spot size: No significant difference was noted between a point source energy beam and a monoenergetic beam of radius 0.50 cm. (See Figure 14 through Figure 17). This had no effect on the on-axis absorbed dose on a material.

Angular divergence: There were no differences noted in the energy and angular spectra of electrons and photons, therefore there were no effect on theon-axis absorbed dose on a material. (See Figure 18 through Figure 21).

Energy smearing: A noticeable difference in the electron energy spectrum was noted when energy smearing was modeled into the simulation. A gradual decrease in the number of electrons per MeV occurred at the higher energy bins for the energy distribution. (See Figure 22 through Figure 25). Energy smearing also had an effect on the dosage pattern of a material. An 18 percent decrease in the absorbed dose was computed when energy smearing was included.

Heavimet Disc vs Production Target: The production target is composed of the composite material heavimet and copper. By adding the copper layer to the simulation, a significant decrease in energy occurs at the higher energy bins and increases at the lower energy bins. The half-width angle for the electron angular spectrum also increased when copper was added. (See Figure 26 through Figure 29).

We have verified the validity of ITS/CYLTRAN simulation codes with great accuracy by dosimetry measurements. Therefore the dose measurements calculated by ITS/CYLTRAN are considered to be more accurate than the data computed using the flash x-ray calculation.

Table 7. RADIATION DOSAGE VALUES AT SM-CO ALLOY: These values are used to plot the radiation dosage pattern for Figure 10 on page 35. Numbers next to each dosage value represents the measure of uncertainty in percent.

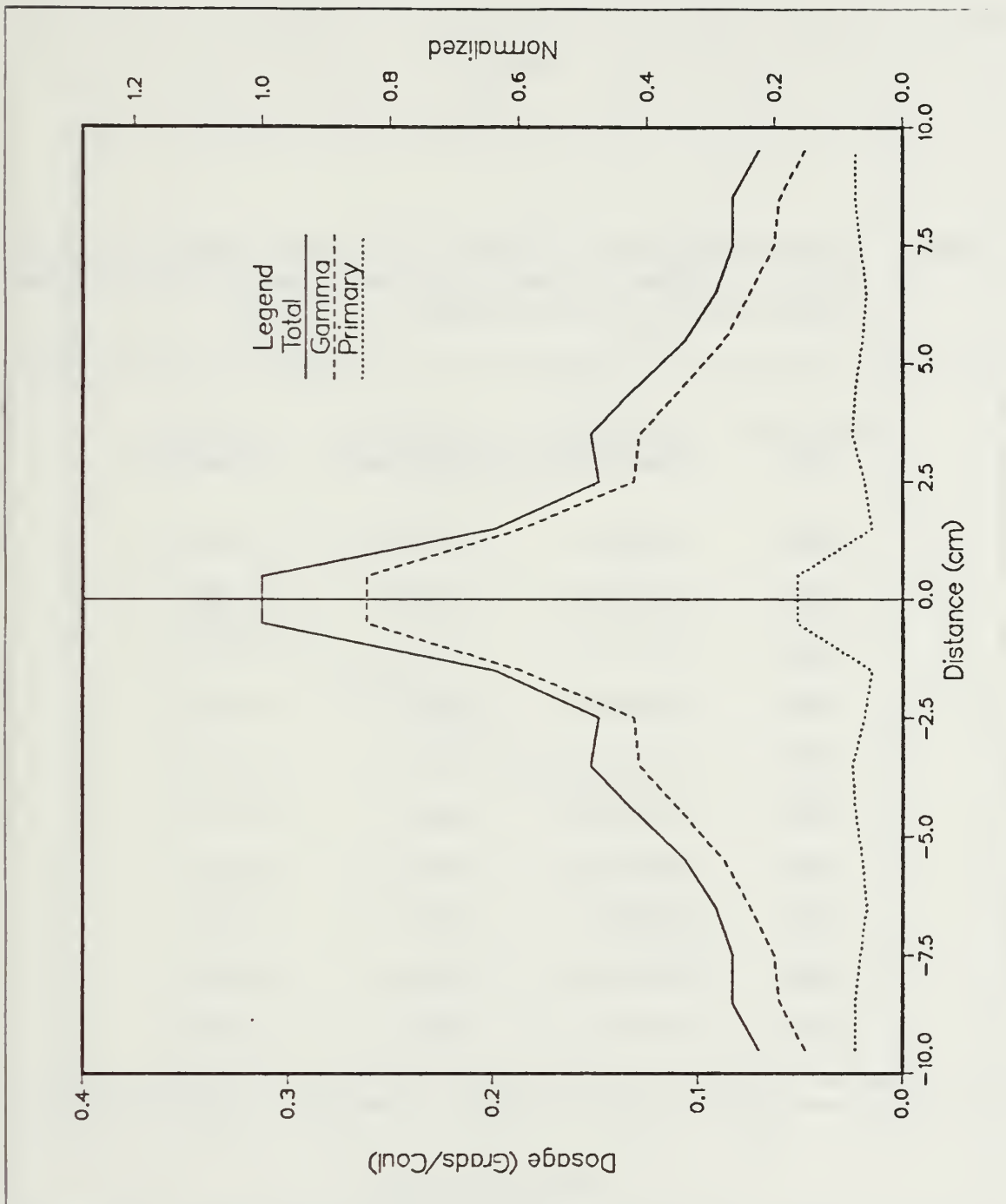| DISTANCE (CM)	PRIMARIES (GRads/Coul)	GAMMAS (GRads/Coul)	TOTAL (GRads/Coul)
0.5000	0.0514 41	0.2613 10	0.3125 11
1.5000	0.0149 26	0.1861 6	0.1988 7
2.5000	0.0186 19	0.1309 8	0.1480 8
3.5000	0.0244 17	0.1282 7	0.1520 6
4.5000	0.0229 14	0.1072 6	0.1298 5
5.5000	0.0194 14	0.0869 5	0.1056 4
6.5000	0.0174 10	0.0742 5	0.0911 5
7.5000	0.0204 13	0.0626 5	0.0828 5
8.5000	0.0230 8	0.0600 4	0.0830 3
9.5000	0.0229 11	0.0476 6	0.0700 6

Figure 10.   Radiation Dosage Pattern at Sm-Co Alloy: The dosage pattern was
calculated using an 85 MeV electron beam with a radius of 0.75 cm.
The absorbing material was positioned 78.7 cm from the production
target based on 10,000 histories.

35

Table 8. **RADIATION DOSAGE VALUES AT ND-FE-B ALLOY:** Same description from Table 7 applies accept values are used to plot the radiation dosage pattern for Figure 11 on page 37.

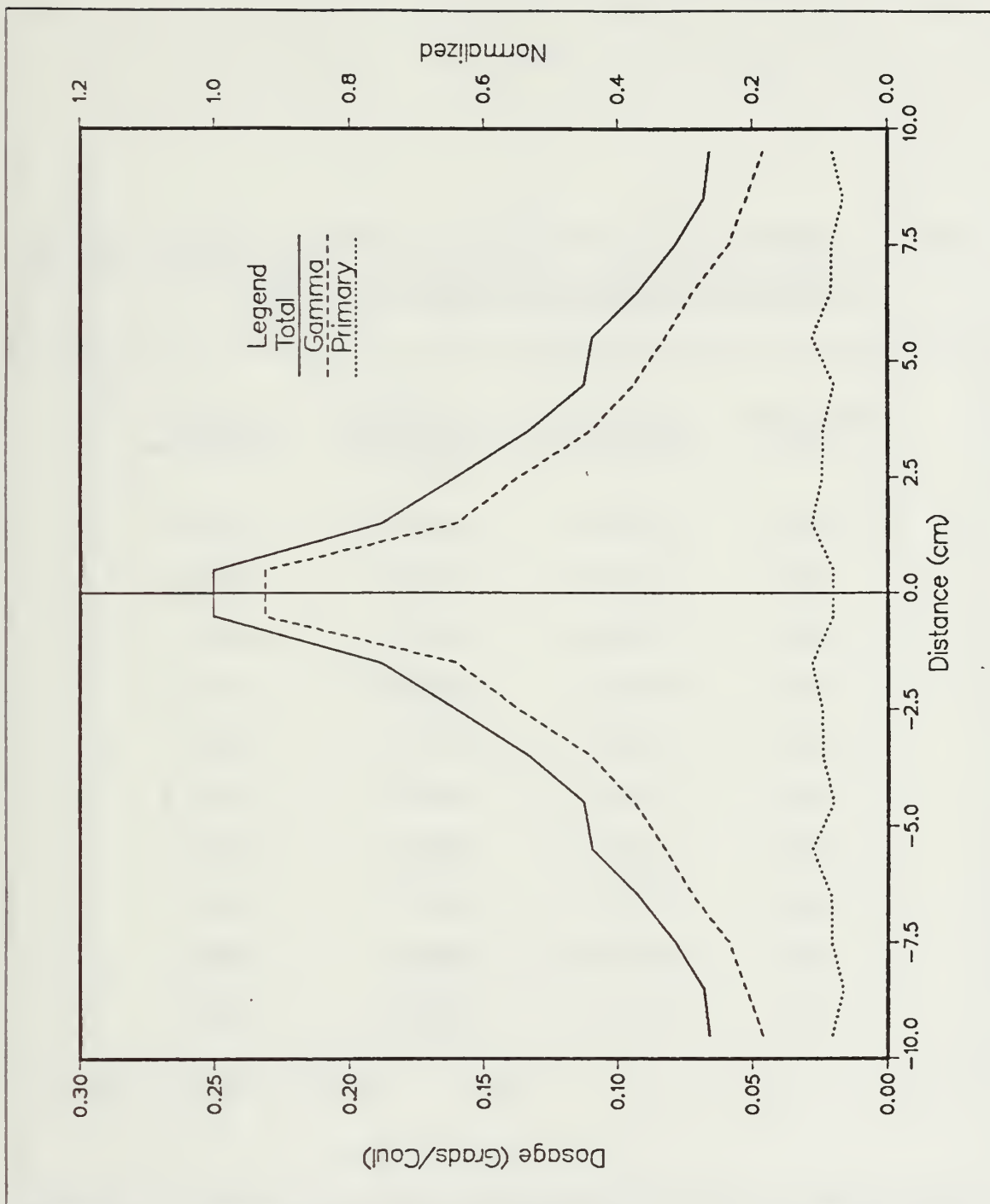| DISTANCE (CM)	PRIMARIES (GRads/Coul)	GAMMAS (GRads/Coul)	TOTAL (GRads/Coul)
0.5000	0.0200 46	0.2311 11	0.2502 12
1.5000	0.0278 25	0.1600 10	0.1880 9
2.5000	0.0241 22	0.1368 9	0.1603 8
3.5000	0.0239 19	0.1097 6	0.1329 5
4.5000	0.0199 19	0.0937 7	0.1124 8
5.5000	0.0277 10	0.0821 7	0.1093 6
6.5000	0.0207 18	0.0717 8	0.0922 7
7.5000	0.0206 10	0.0585 6	0.0783 4
8.5000	0.0162 11	0.0522 6	0.0677 6
9.5000	0.0202 7	0.0460 7	0.0657 5

Figure 11. Radiation Dosage Pattern at Nd-Fe-B Alloy: Same operating parameters as Figure 10 on page 35.

Table 9. **RADIATION DOSAGE VALUES AT PR-FE-B ALLOY:** Same description from Table 7 on page 34 applies accept values are used to plot the radiation dosage pattern for Figure 12 on page 39.

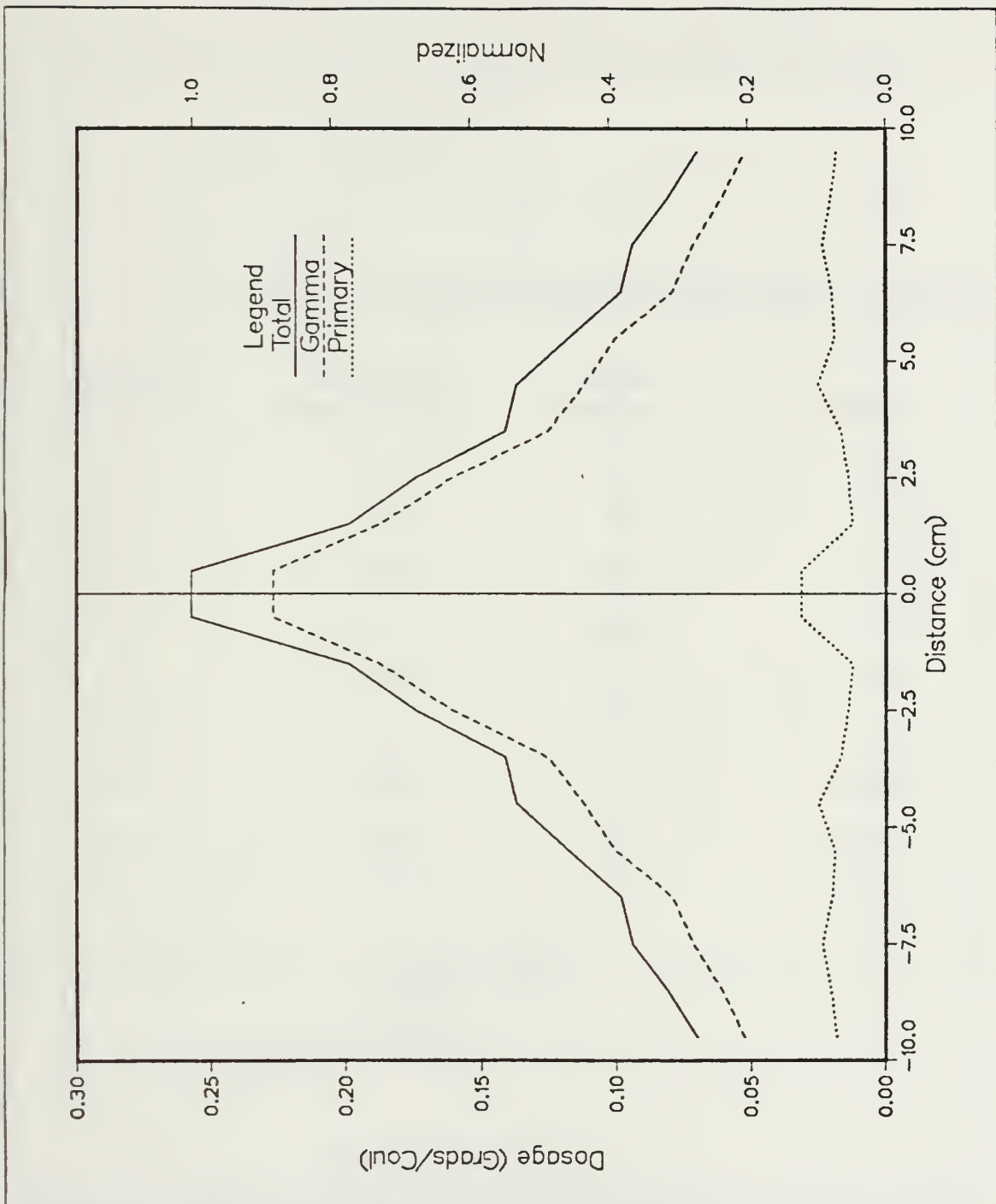| DISTANCE (CM)	PRIMARIES (GRads/Coul)	GAMMAS (GRads/Coul)	TOTAL (GRads/Coul)
0.5000	0.0313 27	0.2267 8	0.2572 8
1.5000	0.0123 36	0.1874 10	0.1988 9
2.5000	0.0139 24	0.1606 4	0.1741 4
3.5000	0.0167 15	0.1252 6	0.1410 6
4.5000	0.0250 17	0.1119 7	0.1369 7
5.5000	0.0189 16	0.1001 5	0.1178 5
6.5000	0.0199 9	0.0790 4	0.0982 5
7.5000	0.0234 8	0.0713 6	0.0939 4
8.5000	0.0203 11	0.0606 4	0.0808 5
9.5000	0.0181 11	0.0523 5	0.0699 4

Figure 12.   Radiation Dosage Pattern at Pr-Fe-B Alloy: Same operating parameters as Figure 10 on page 35.

Table 10. DOSAGE ON VARIOUS MATERIALS

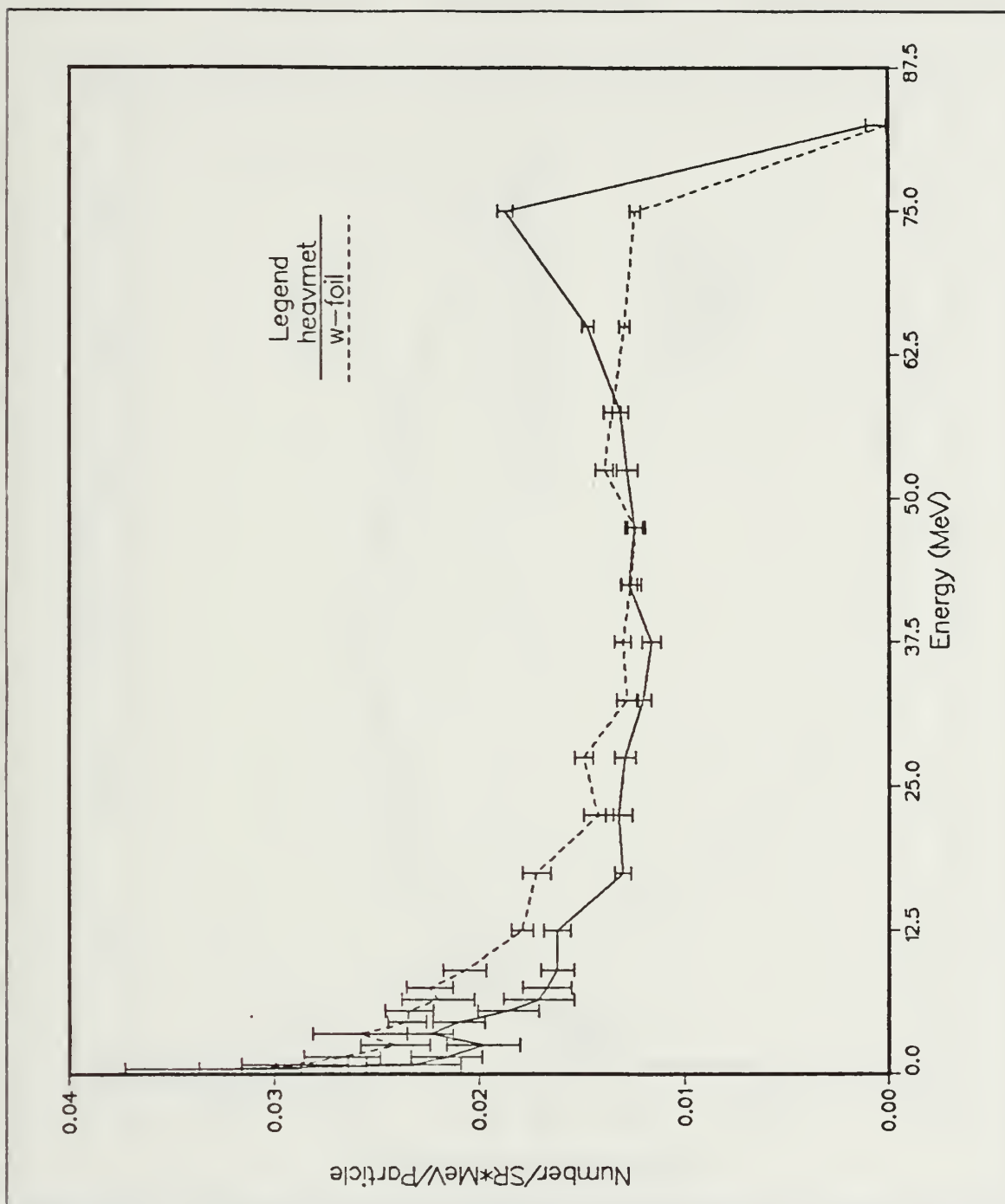| Material	Density (gr/cm³)	On-axis Dose (x 10⁹ rads/coul)	Dose Relative to Silicon
Ca	1.55	0.104	0.97
Si	2.33	0.107	1.00
LiF	2.69	0.084	0.79
Ni	8.90	0.352	3.29
Co	8.83	0.347	3.24
Fe	7.87	0.300	2.80
Sm_2Co_{17}	8.38	0.289	2.70
$Nd_2Fe_{14}B$	7.60	0.250	2.34
$Pr_{15}Fe_{79}B_6$	10.20	0.285	2.66

Figure 13. Tungsten vs Heavimet Electron Energy Spectrum: The spectrum was calculated using an 85 MeV electron beam with a radius of 0.50 cm. The absorbing material was positioned 78.7 cm from the production target based on 10,000 histories.
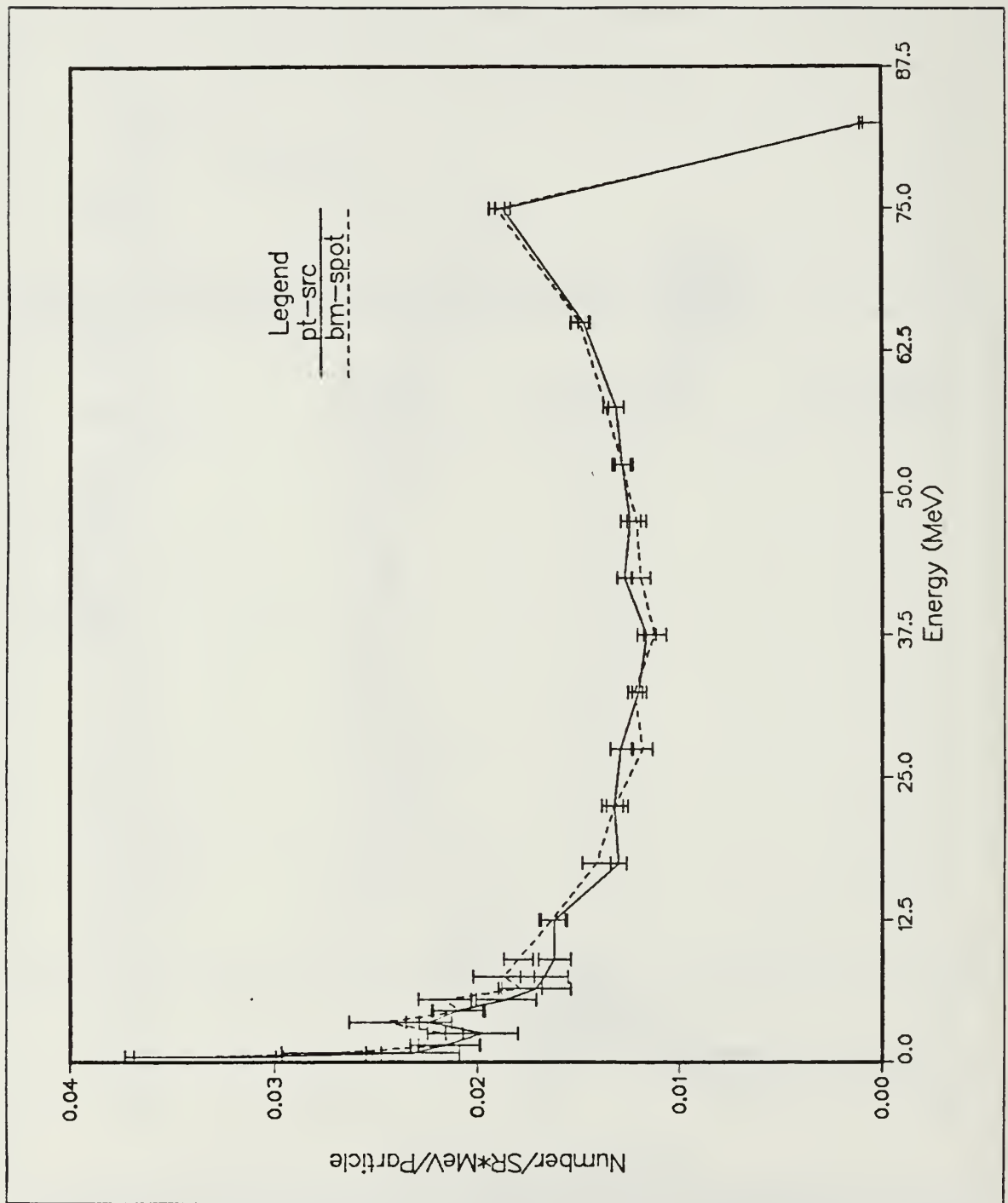
Figure 14.   Point   Source   vs   Monoenergetic   Beam   Electron   Energy
Spectrum: Same operating parameters as Figure 13 on page 41 used
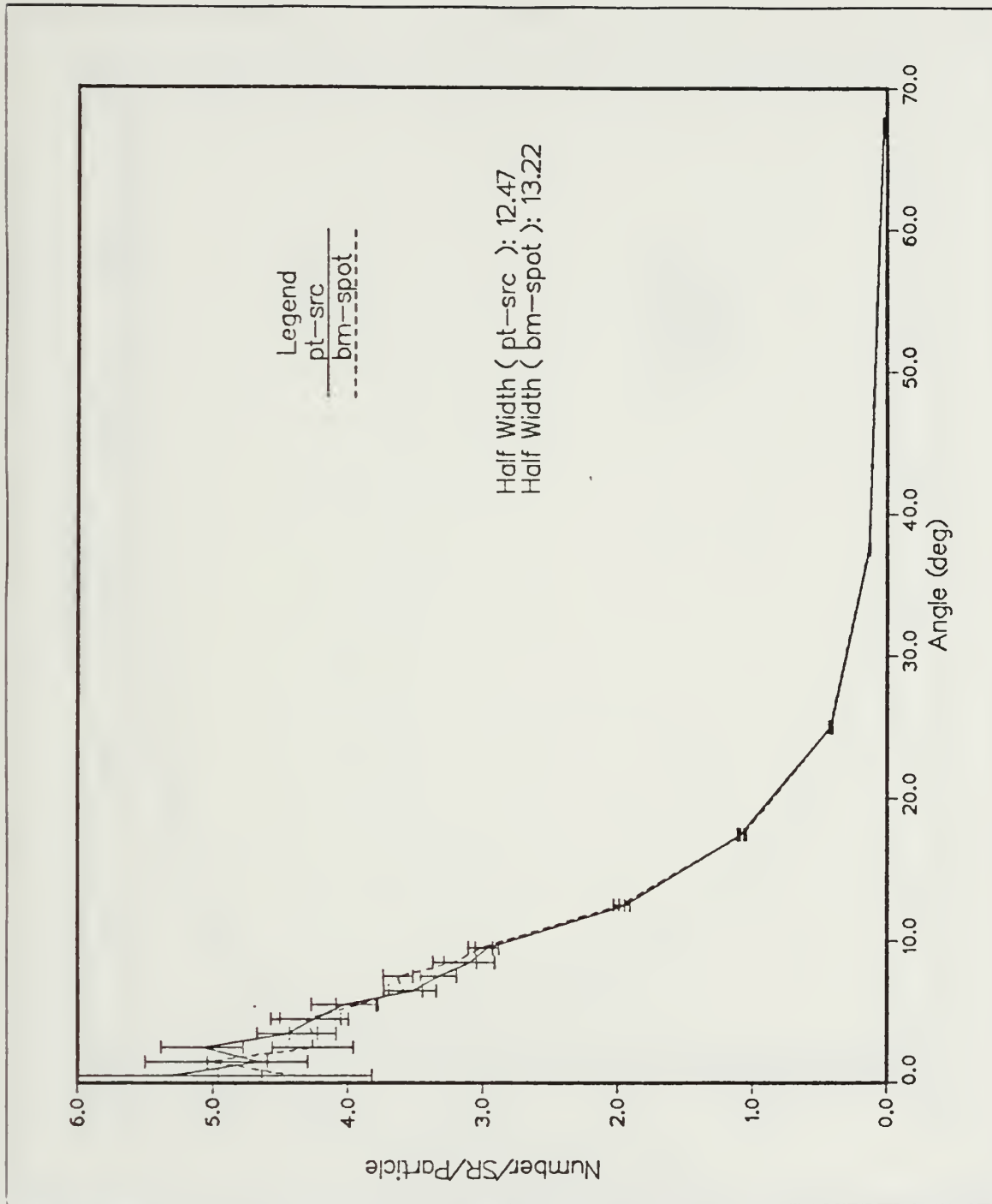to compare a point source beam with a monoenergetic beam of radius
0.50 cm.

Figure 15. Point Source vs Monoenergetic Beam Electron Angular Spectrum: Same operating parameters as Figure 14 on page 42.
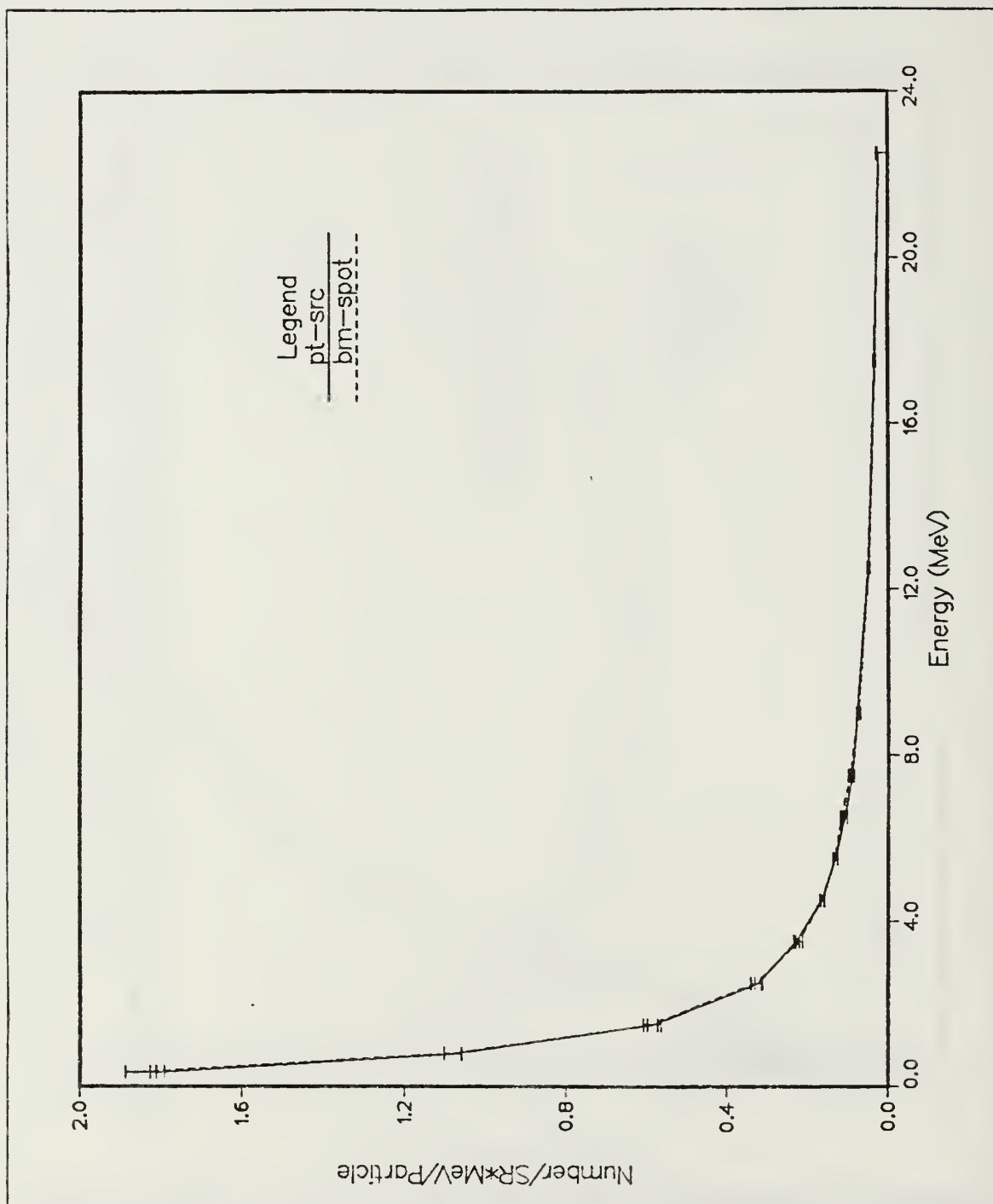
43

Figure 16.   Point Source vs Monoenergetic Beam Photon Energy Spectrum: Same operating parameters as Figure 14 on page 42.
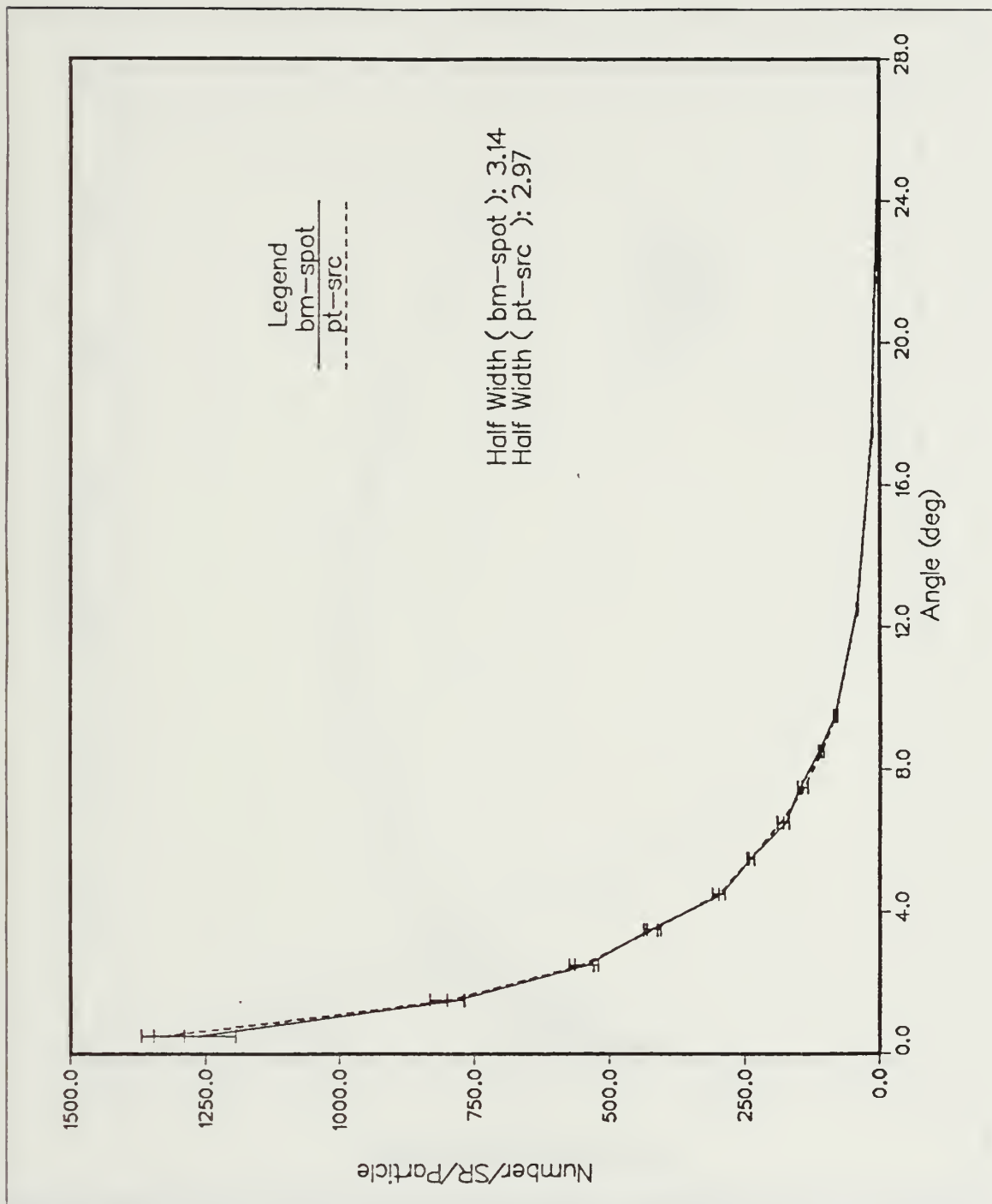
Figure 17.   Point   Source   vs   Monoenergetic   Beam   Photon   Angular
           Spectrum: Same operating parameters as Figure 14 on page 42.

45

Figure 18. Angular Divergence Comparison for Electron Energy Spectrum: Same operating parameters as Figure 14 on page 42 accept a divergence angle of 0.18° was incorporated into the simulation. Comparison was made with a monoenergetic beam without angular divergence.

Figure 19. Angular Divergence Comparison for Electron Angular Spectrum: Same operating parameters as Figure 18 on page 46.

Figure 20.   Angular Divergence Comparison for Photon Energy Spectrum: Same operating parameters as Figure 18 on page 46.
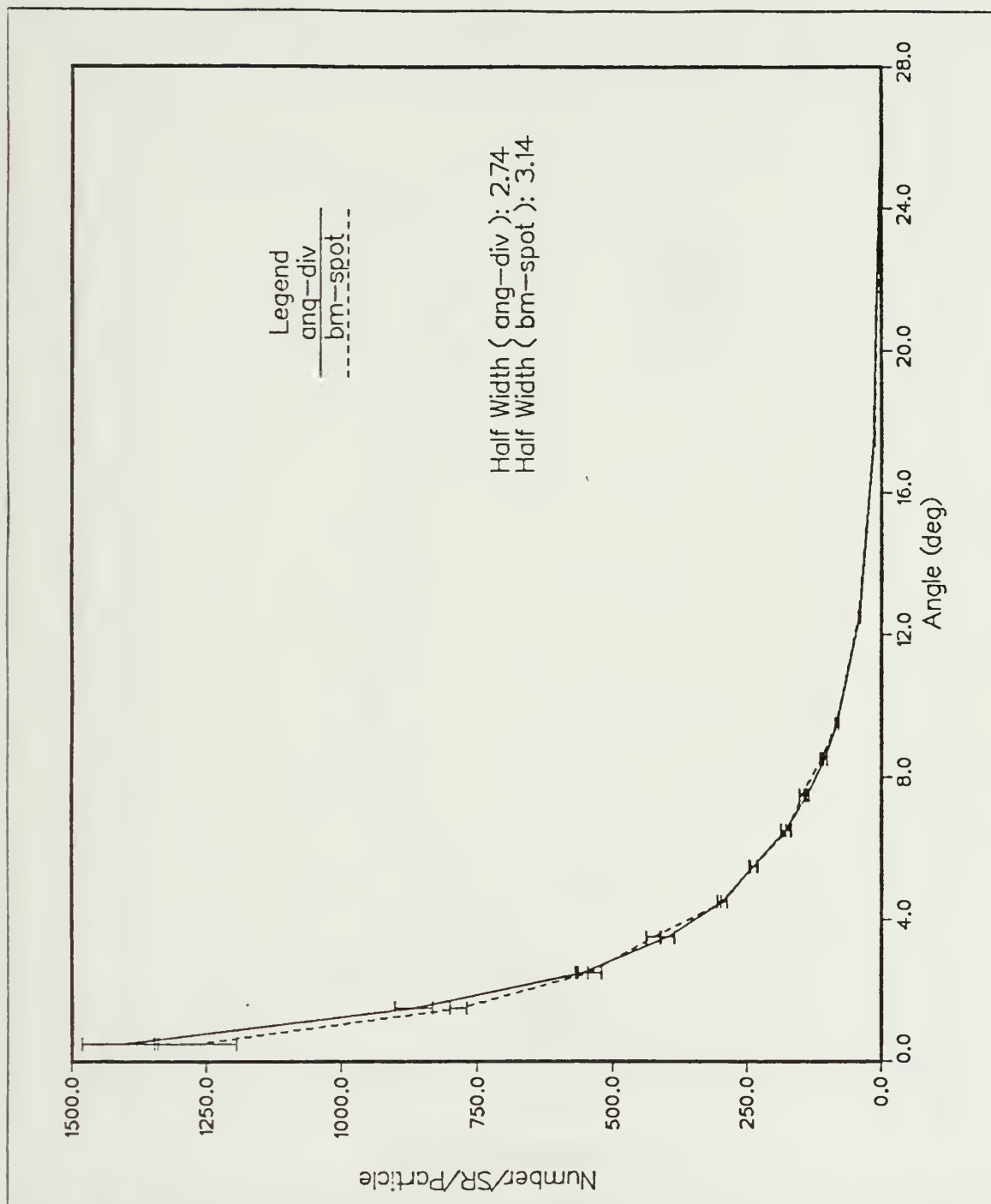
Figure 21. Angular Divergence Comparison for Photon Angular Spectrum: Same operating parameters as Figure 18 on page 46.
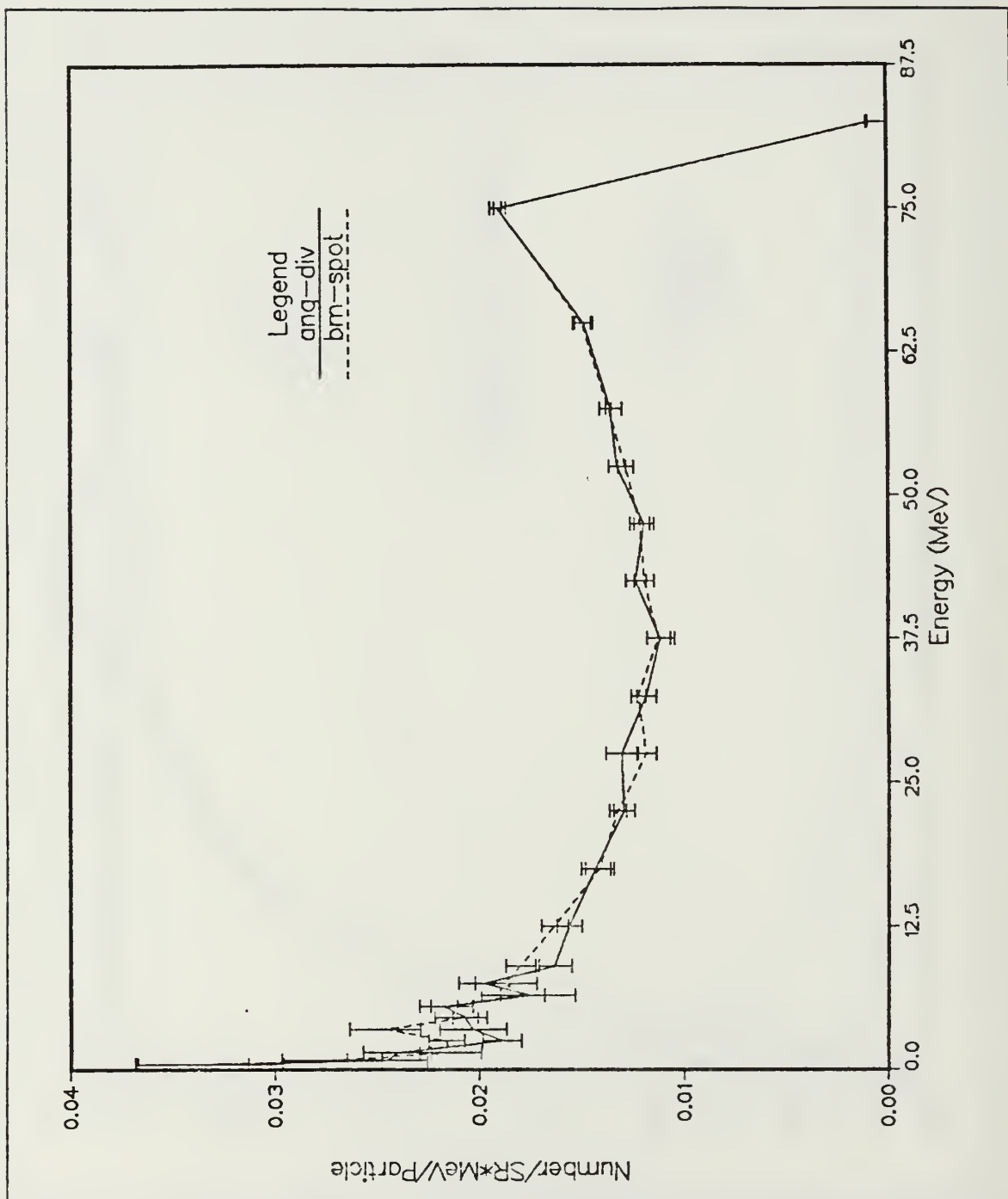
49
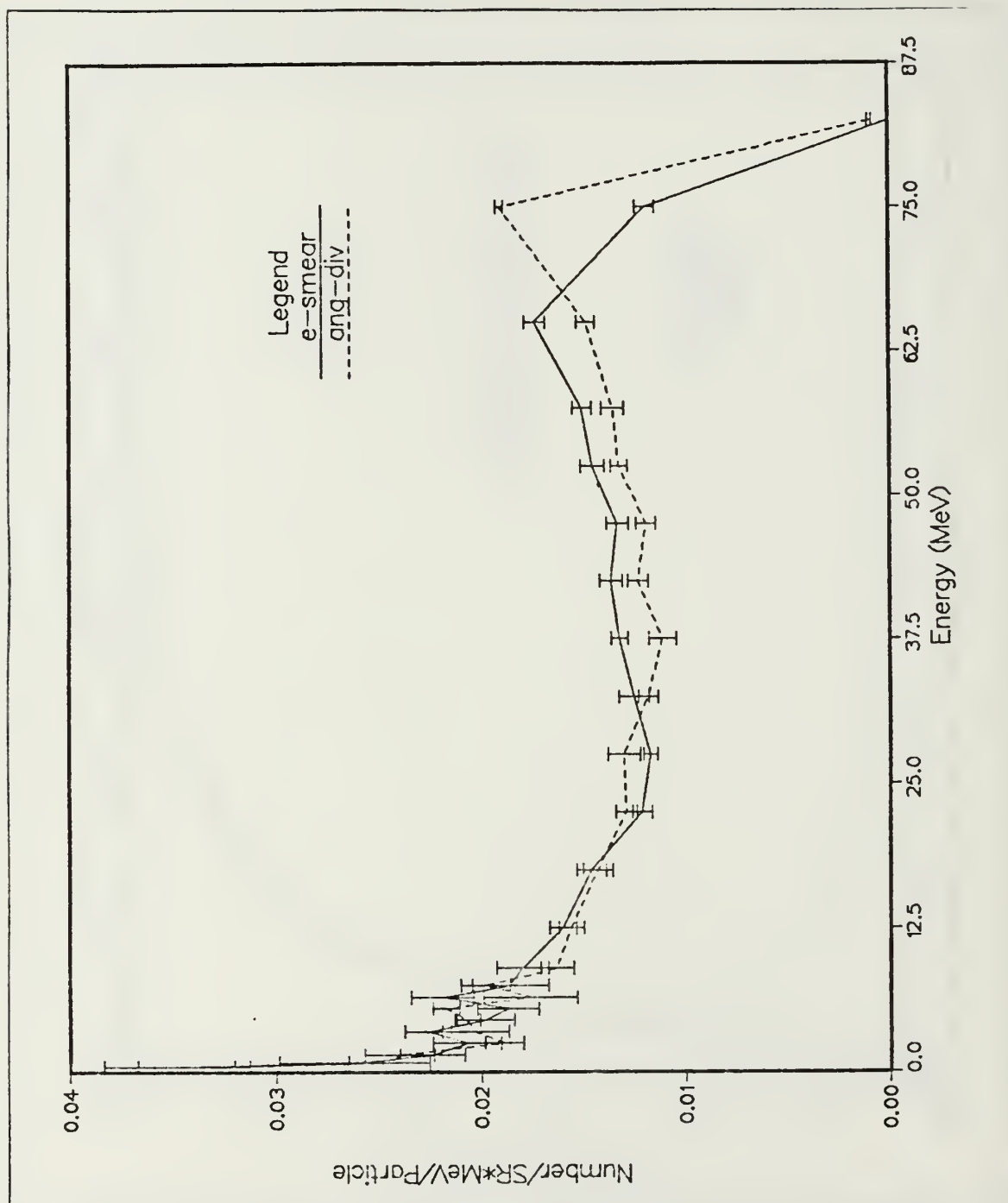
Figure 22.   Energy Smearing Comparison for Electron Energy Spectrum: Same operating parameters as Figure 18 on page 46 accept a divergence angle of 0.18° and five percent energy smearing was incorporated into the simulation.   Comparison was made with a monoenergetic beam with angular divergence.
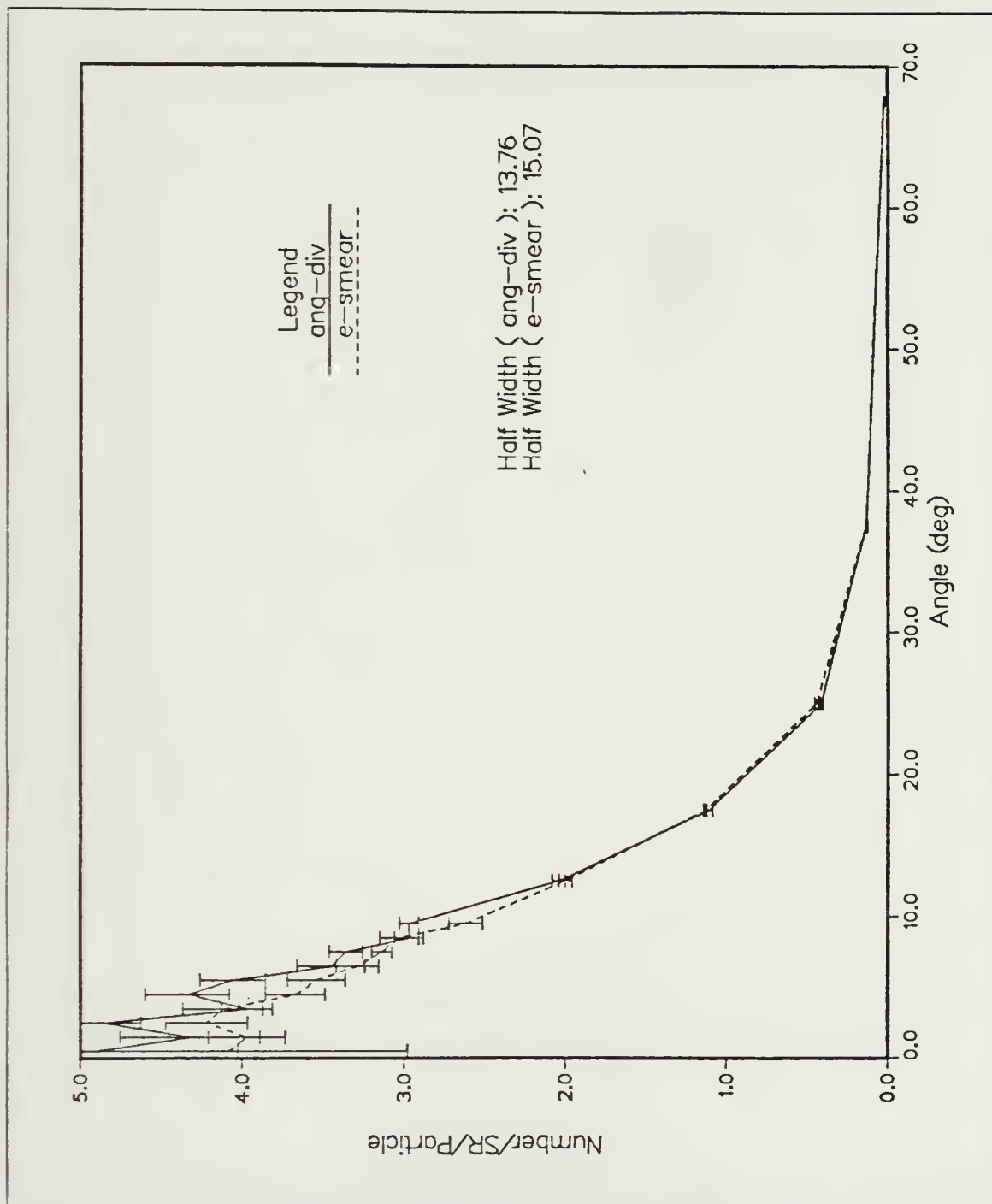
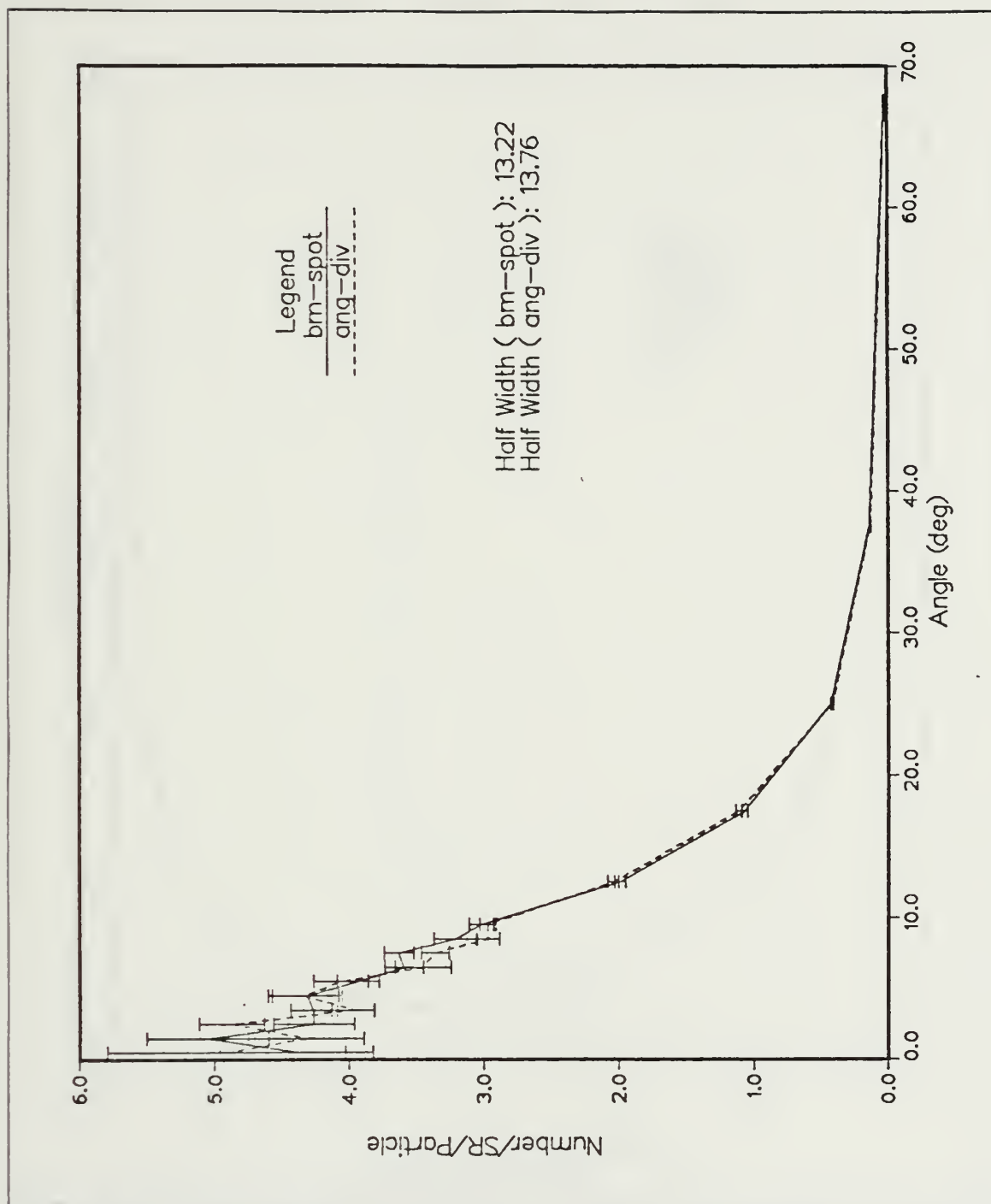Figure 23. Energy Smearing Comparison for Electron Angular Spectrum: Same operating parameters as Figure 22 on page 50.

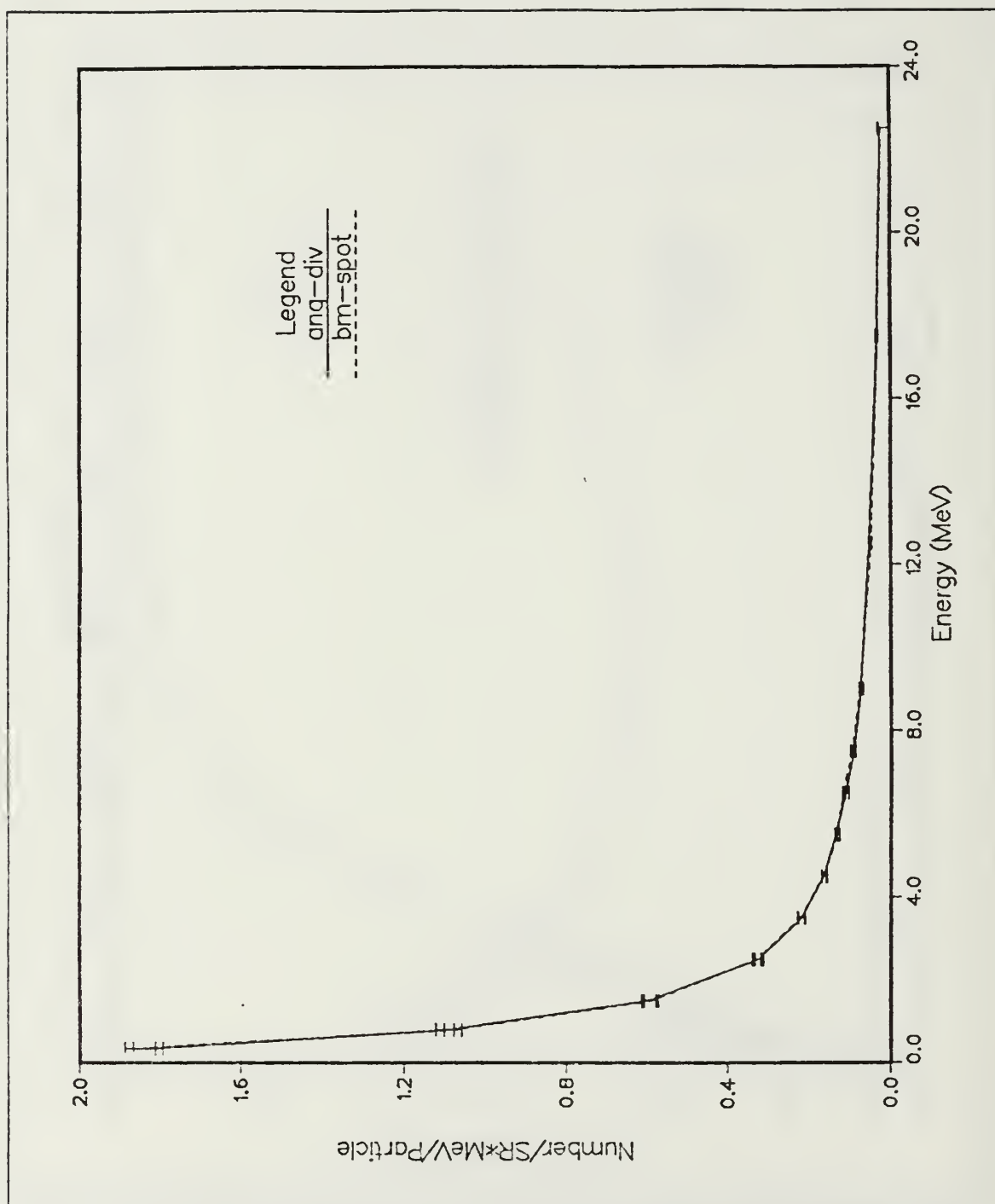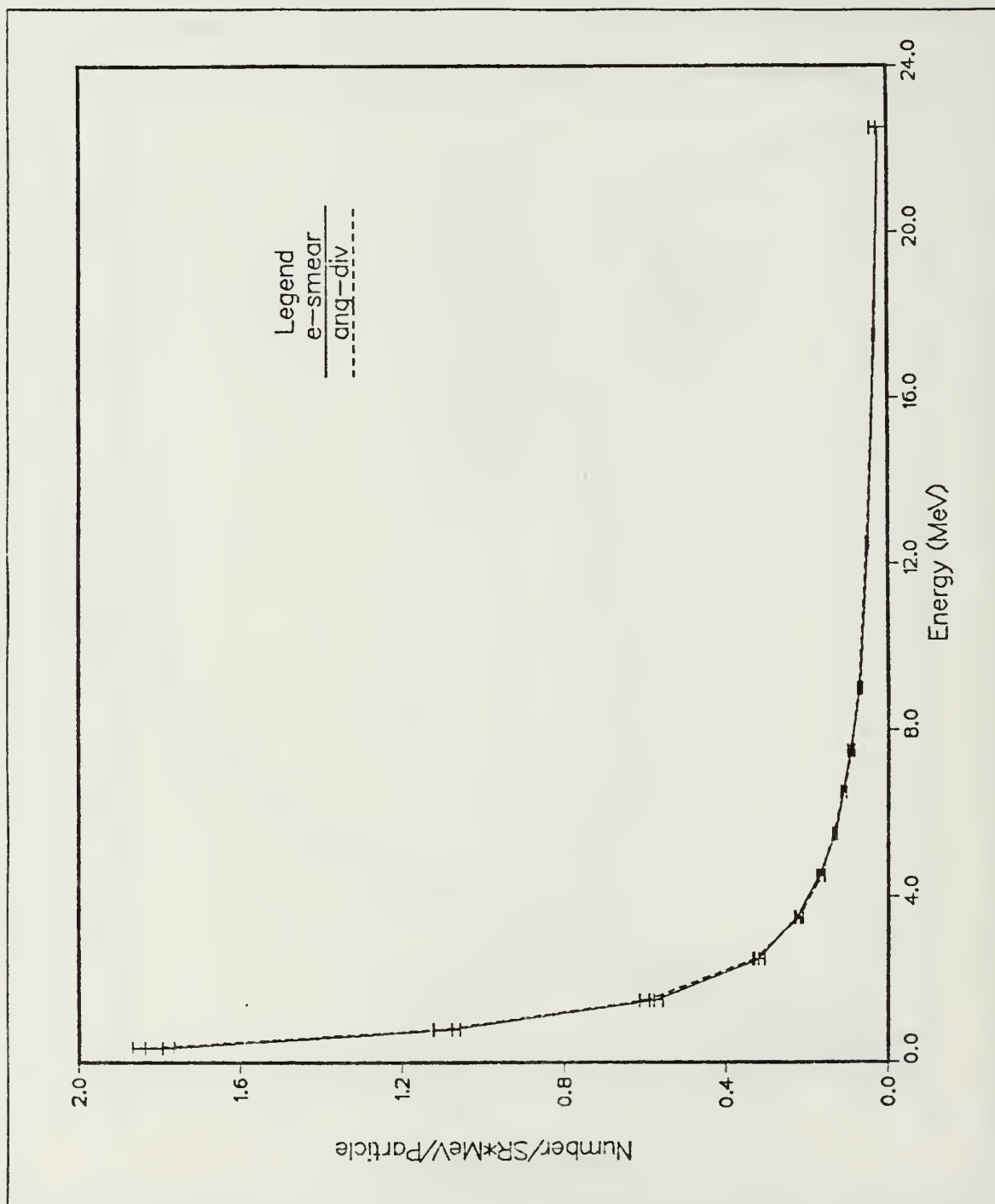Figure 24.   Energy Smearing Comparison for Photon Energy Spectrum: Same operating parameters as Figure 22 on page 50.
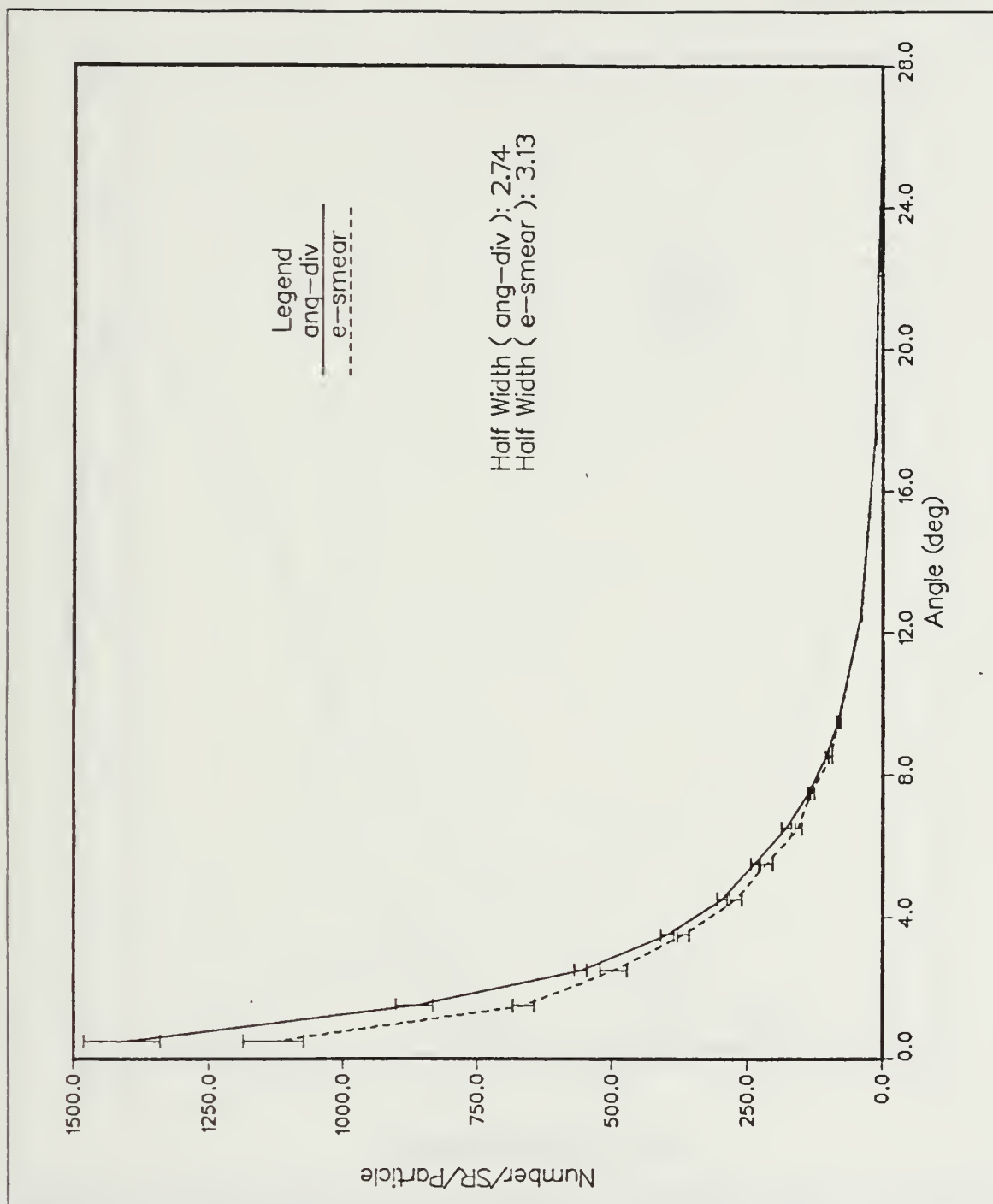
Figure 25.   Energy Smearing Comparison for Photon Angular Spectrum: Same operating parameters as Figure 22 on page 50.
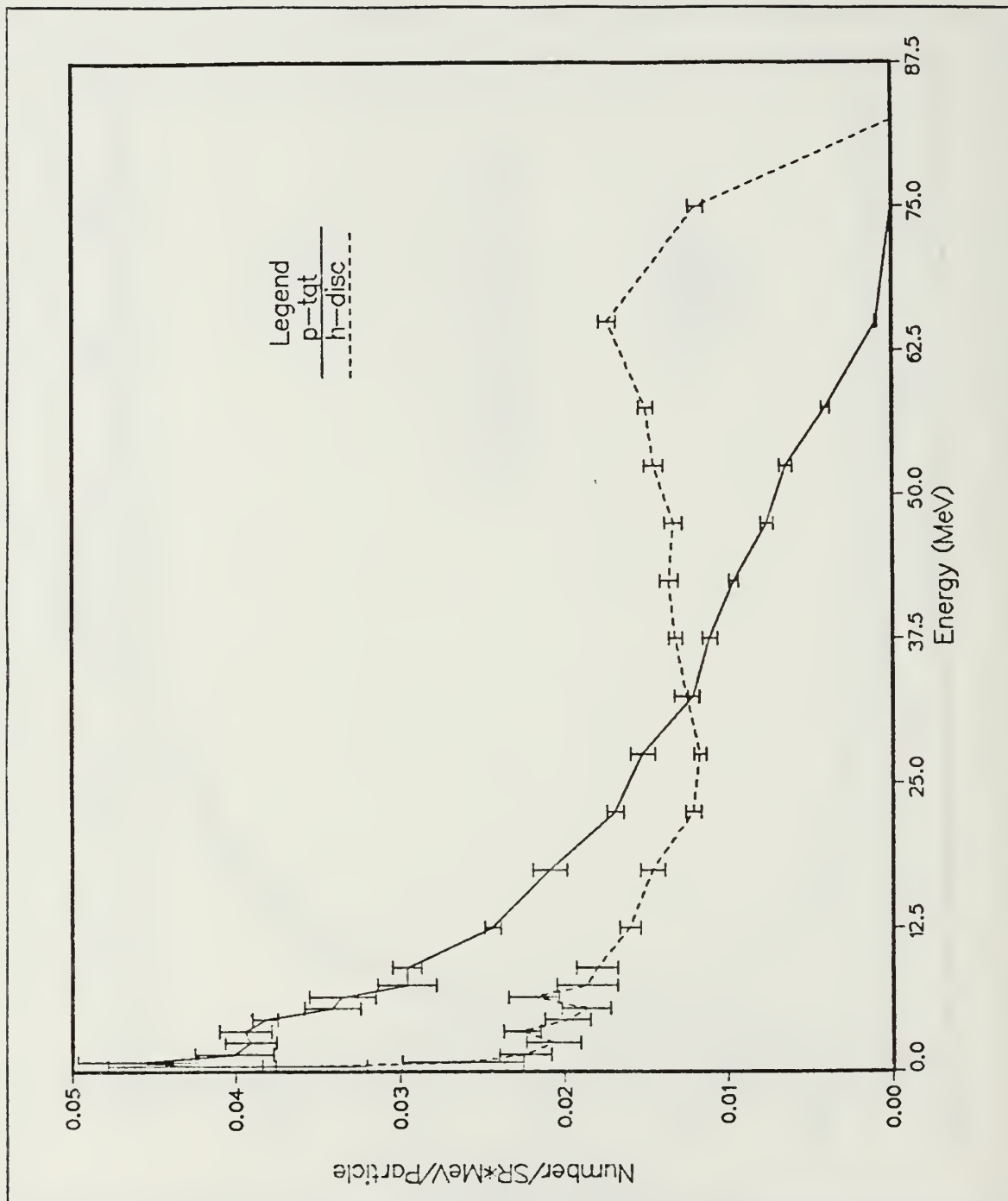
Figure 26.   Heavimet Disc vs Production Target Electron Energy Spectrum: Same operating parameters as Figure 22 on page 50. Compares spectra with 0.80 cm copper lining added to the production target.
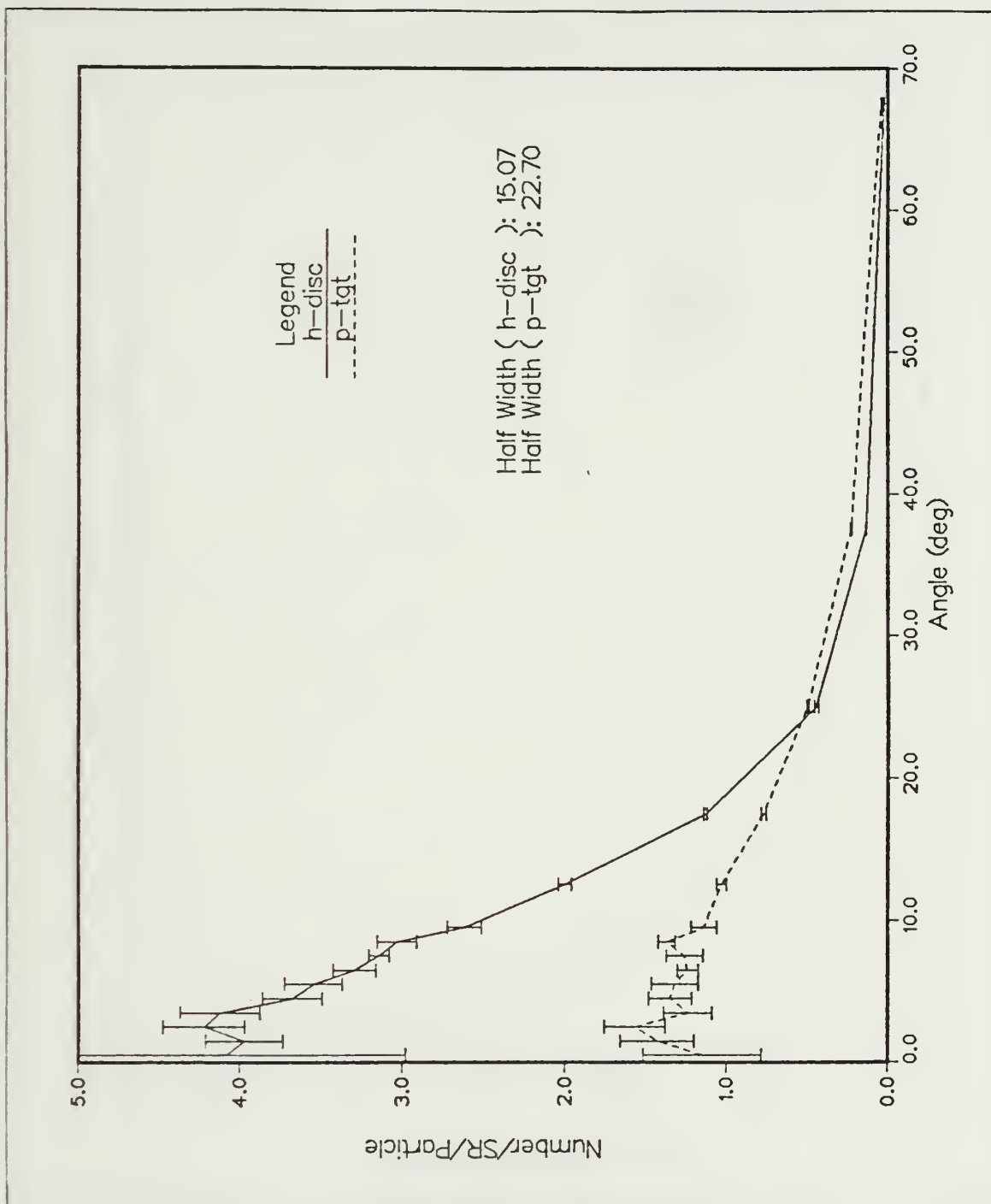
Figure 27.   Heavimet   Disc   vs   Production   Target   Electron   Angular
Spectrum: Same operating parameters as Figure 26 on page 54.

55
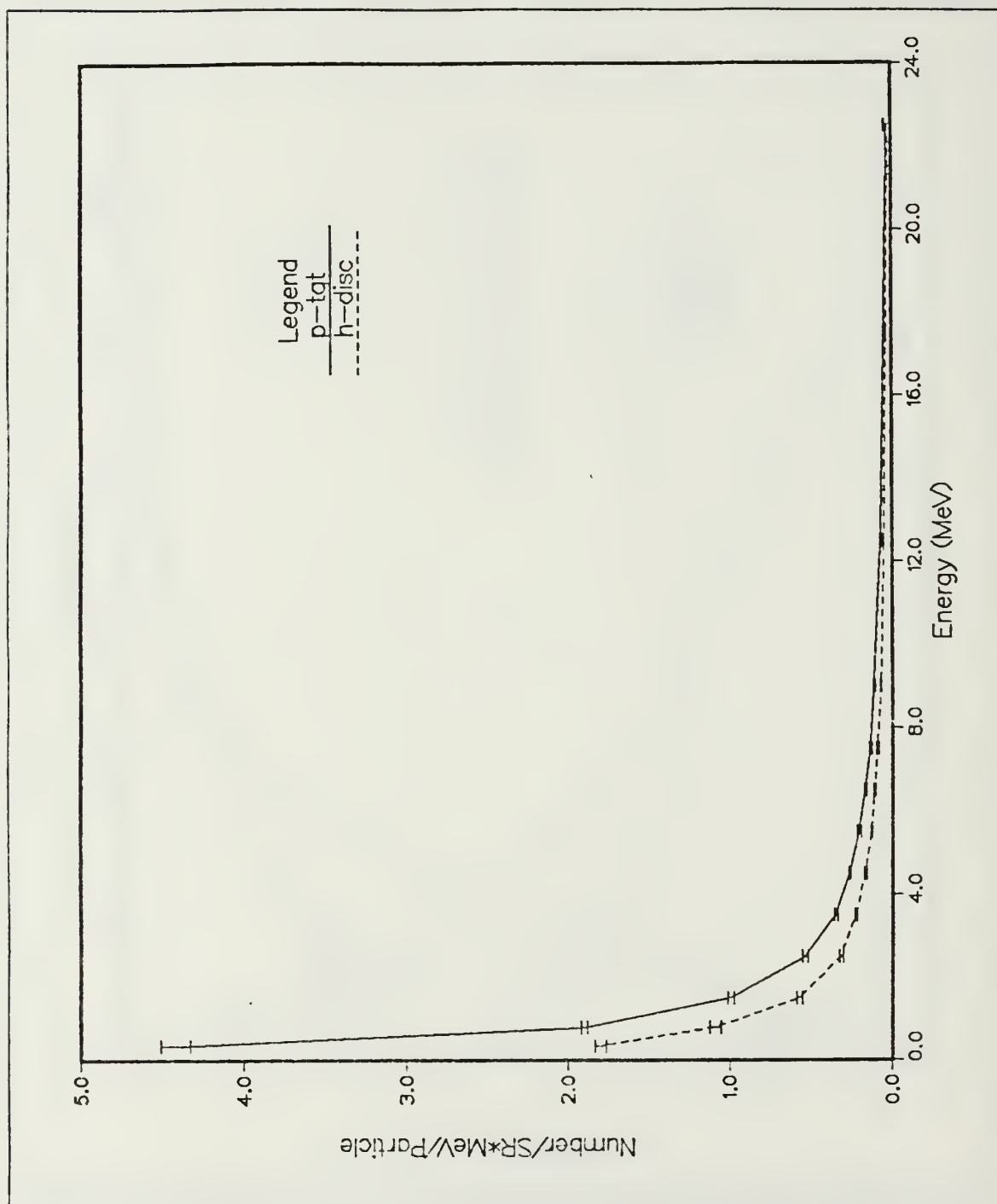
Figure 28.   Heavimet Disc vs Production Target Photon Energy Spectrum: Same operating parameters as Figure 26 on page 54.
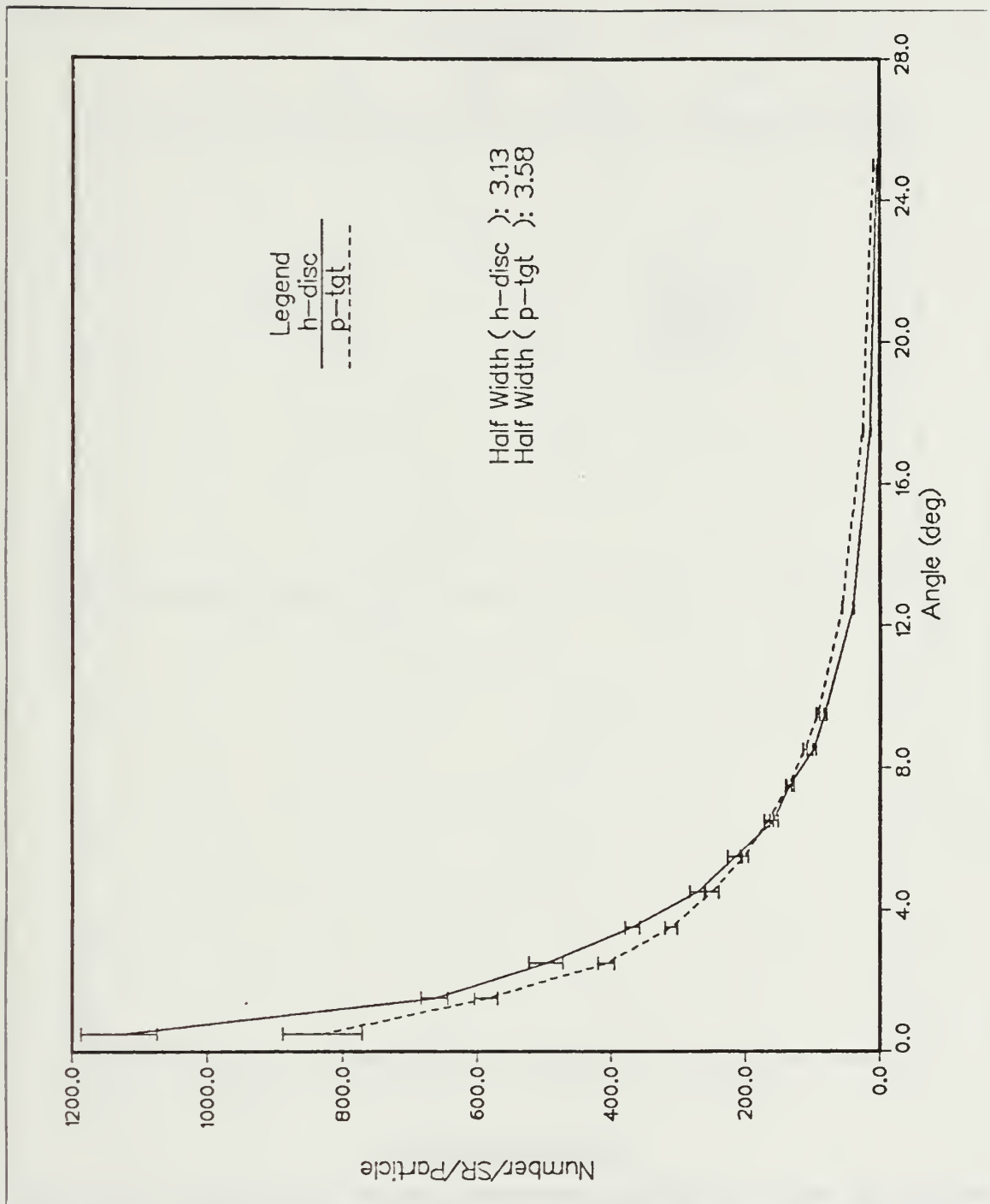
Figure 29. Heavimet Disc vs Production Target Photon Angular Spectrum: Same operating parameters as Figure 26 on page 54.
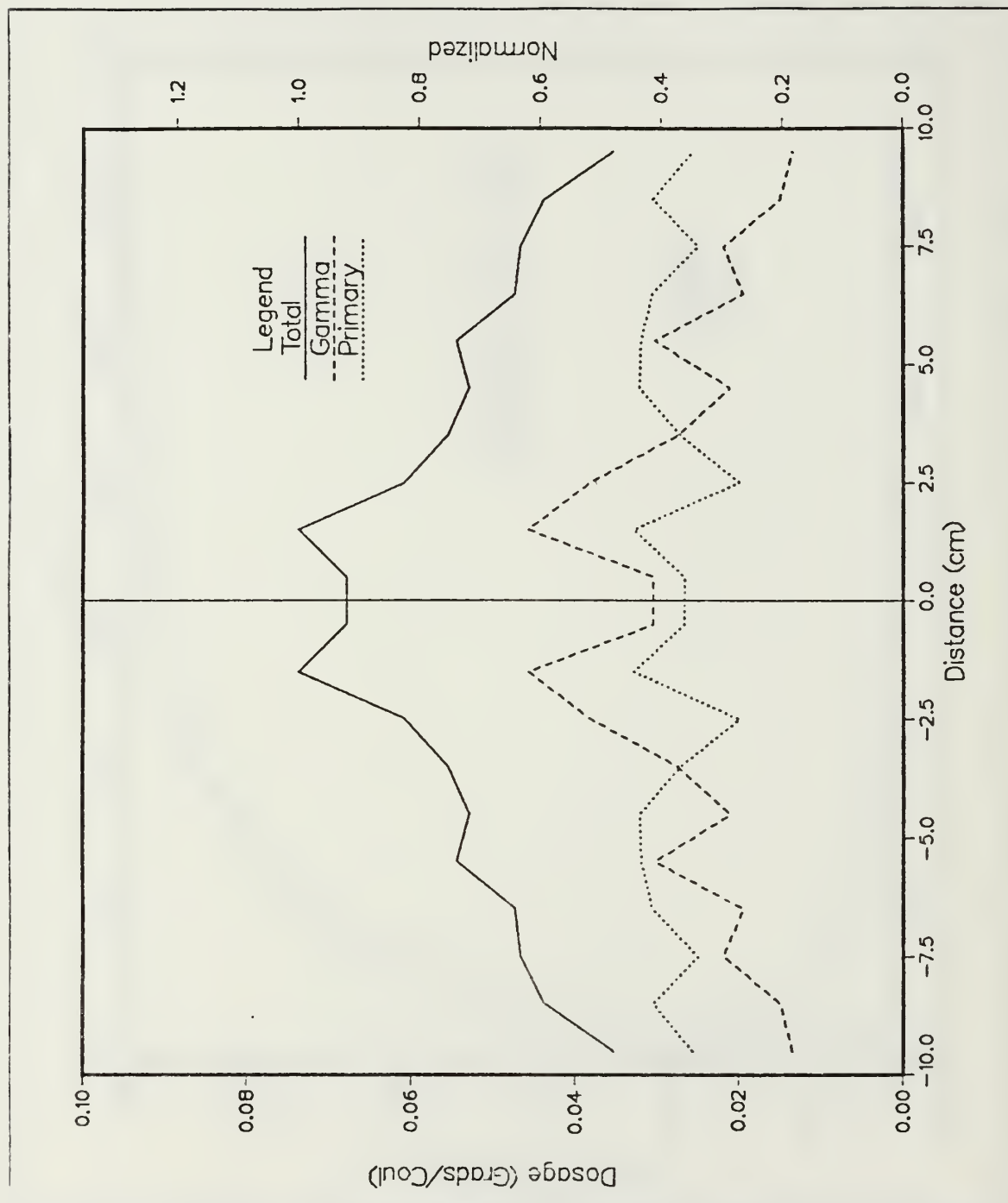
Figure 30. Radiation Dosage Pattern for LiF with a Halo Effect: The dosage pattern was calculated using an 85 MeV electron beam with a radius of 1.00 cm. The absorbing material was positioned 78.7 cm from the production target based on 10,000 histories.
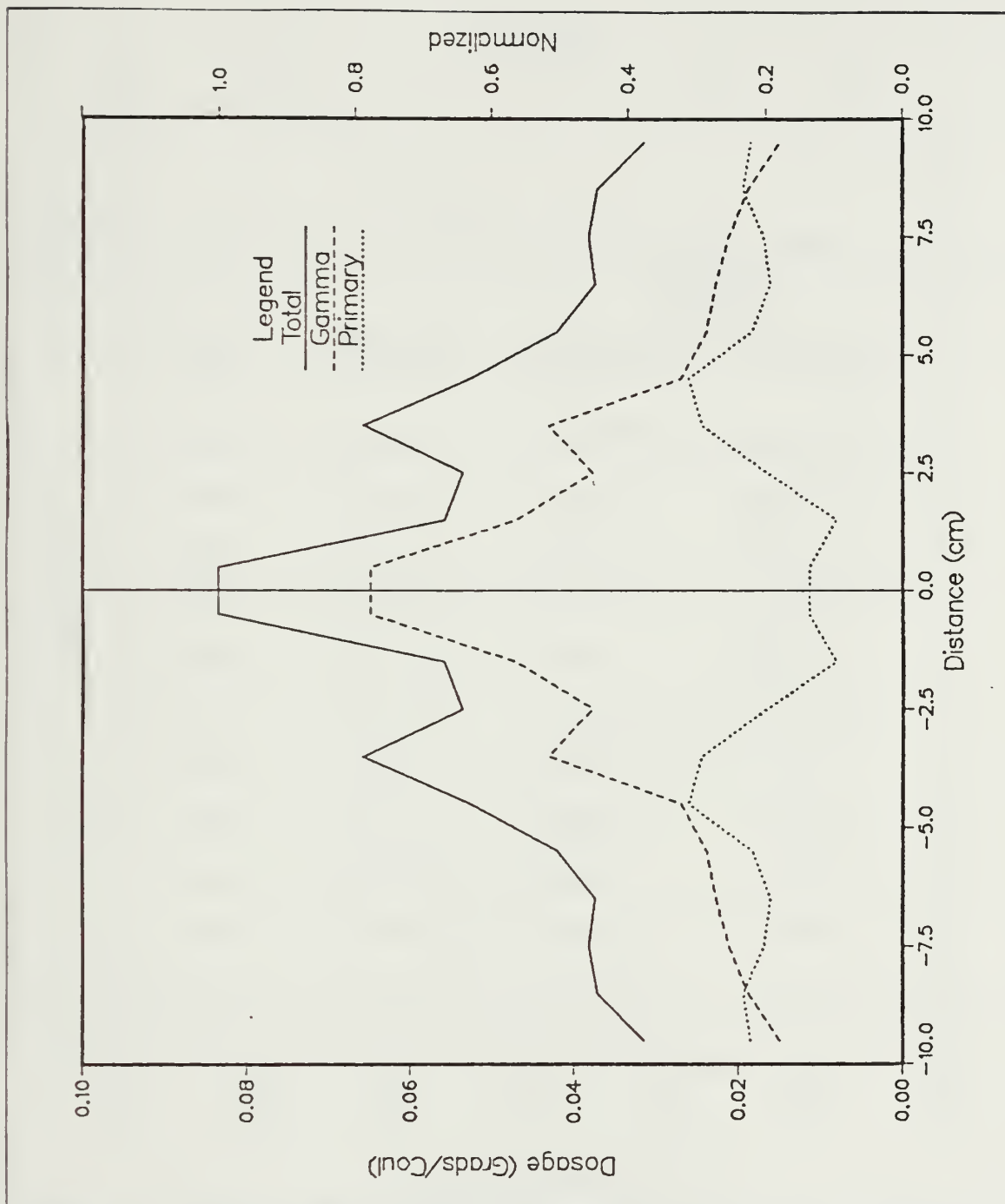
Figure 31.   Radiation Dosage Pattern for LiF without a Halo Effect: Same oper-
ating parameters as Figure 30 on page 58 accept beam radius of 0.75
cm was simulated.
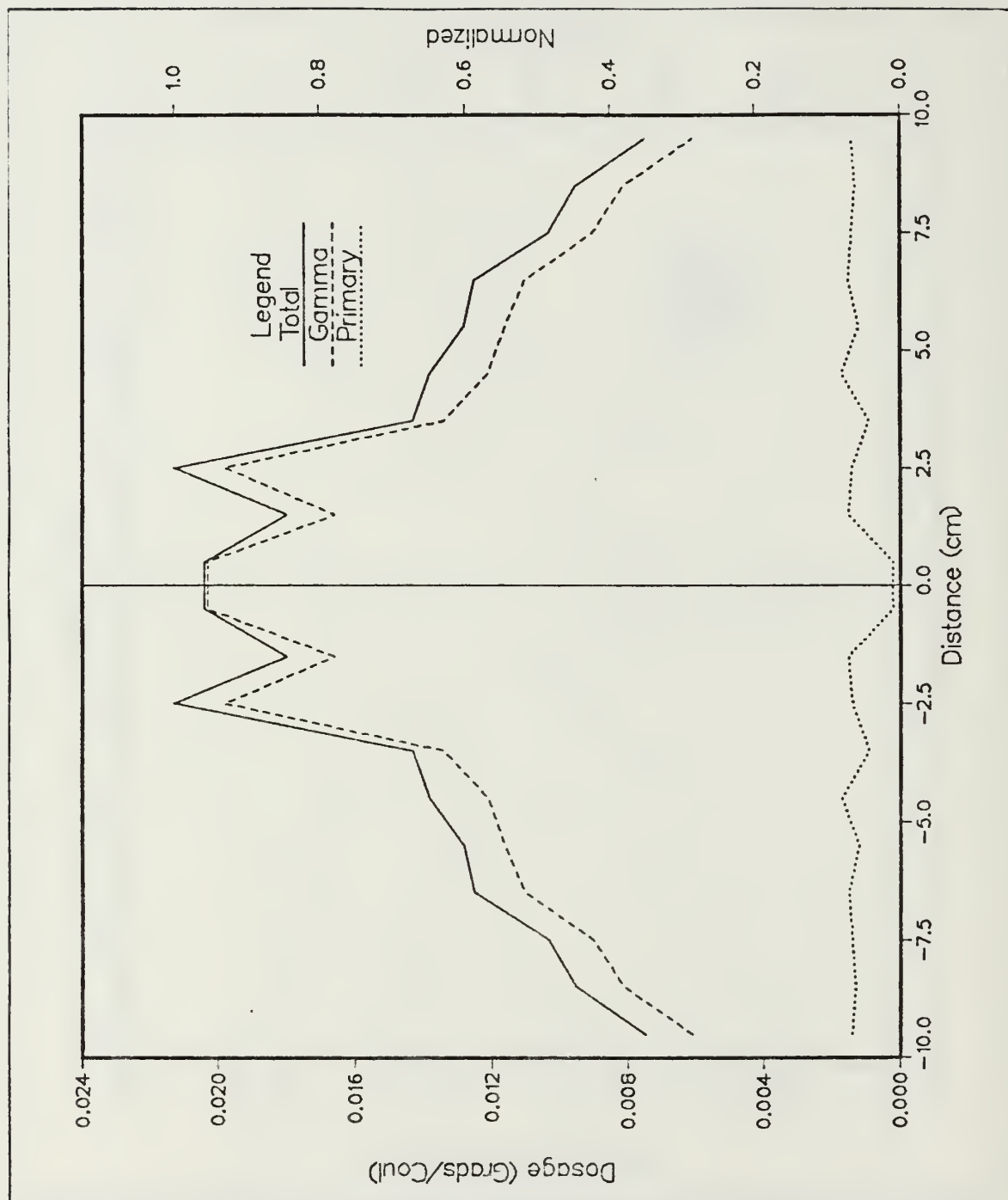
Figure 32. Verification of the Radiation Dosage Pattern for LiF: The dosage pattern was calculated using an 85 MeV electron beam with a radius of 0.75 cm. The absorbing material was positioned 167.8 cm from the production target based on 10,000 histories.

Table 11. RADIATION DOSAGE VALUES FOR LIF TLD CHIPS

DISTANCE (CM)	PRIMARIES (GRads/Coul)		GAMMAS (GRads/Coul)		TOTAL (GRads/Coul)	
0.5000	0.0002	90	0.0203	18	0.0204	18
1.5000	0.0015	61	0.0166	8	0.0180	8
2.5000	0.0014	44	0.0198	7	0.0213	5
3.5000	0.0009	34	0.0134	6	0.0143	6
4.5000	0.0017	18	0.0121	5	0.0138	4
5.5000	0.0012	27	0.0116	6	0.0128	6
6.5000	0.0015	27	0.0110	7	0.0125	7
7.5000	0.0014	31	0.0090	8	0.0103	10
8.5000	0.0013	22	0.0081	8	0.0095	7
9.5000	0.0014	32	0.0061	10	0.0075	8

V. CONCLUSIONS

After radiating a total of 21 permanent magnet samples from four different manufacturers and exposing them to bremsstrahlung doses of up to 1.8 gigarads, the following conclusions can be made based on the irradiation runs conducted at LLNL's 100 MeV Linac:

1. Sm_2Co_{17} was found to be significantly less sensitive to gamma radiation than $Nd_2Fe_{14}B$, which agrees with previous neutron and proton irradiation experiments.

2. Temperature effects were insignificant and did not contribute to the magetization loss of any sample. For the initial irradiation runs, the temperature of each sample was maintained near room temperature by a water-cooling system. An out-of-beam reference magnet which was not water cooled during the irradiation runs, measured no loss in remanence. The monitored temperature at the reference magnet measured slightly above room temperature of 28 °C. We can therefore conclude that temperature did not reach a level high enough to cause remanence losses.

3. The samples of $Nd_2Fe_{14}B$ were provided by two different manufacturers, Hitachi Magnetics Corporation (Hicorex 94EB) and Crucible Magnetics Company (Crumax 355). The Hicorex 94EB samples lost three to five percent of their original remanence compared to only a one to two percent drop for the Crumax 355 after absorbing a maximum dose of 0.92 gigarads. Samples from different manufacturers exhibit large differences in the demagnetization as a function of dose. Different production processes, the presence of different alloy additives or the microcrystalline structure could be responsible for the difference in the rate of remanence loss.

4. The sample alloy of $Pr_{15}Fe_{79}B_6$ proved to be extremely sensitive to gamma radiation losing 75% of it original remanence after absorbing a maximum dose of 1.78 gigarads.

Future studies should further explore these trends. Development of new magnetic materials have provided a more promising outlook in magnet technology. The manufacturers of permanent magnets should continue to provide new material samples to

radiation facilities to continue this field of research and determine the optimum permanent magnet for use in high radiation environments. As the data base expands, phenomenological models, which address microstructural factors may evolve to levels that provide guidelines for the manufacture of radiation resistant alloys. A comprehensive program to assess phenomenology of many types of magnets would benefit from the use of an automated remote "in-situ" magnetometer.

The ITS analysis of the experimental data obtained from the irradiation runs proved to be extremely valuable. The comparisons between measured results and ITS simulation runs showed high levels of agreements. This proved that ITS can be utilized more extensively to analyze similar models and achieve useful results. With the operating cost of irradiation time steadily increasing, utilization of the ITS/CYLTRAN Monte Carlo simulation codes to analyze energy deposition, energy and angular distributions can prove extremely economical. More sophisticated simulation codes, which utilizes the same Monte Carlo scheme to calculate electron, photon and neutron spectra are in use today. By taking advantage of these resources, more in-depth analysis of radiation effects can be conducted at significantly lower cost.

Permanent magnet technology and their applications have grown to become a $1 billion industry. Though improvements in the quality and strength of magnetic materials continue, Sm_2Co_{17} still remains the best suited magnet compound for high radiation environment.

Based on our recent study and the previous studies conducted at LANL, CERN and TRIUMPF, these radiation damage experiments lead us to the empirical observation that the order of radiation hardness is Sm_2Co_{17}, $SmCo_5$ and $Nd_2Fe_{14}B$, regardless of the source of radiation, i.e. gammas, electrons, protons and neutrons.

APPENDIX A.   MAGNETIC PROPERTIES OF MATERIALS

The following concepts and terminologies of magnetic properties are provided to aid the reader in obtaining an introductory understanding of magnetic materials. The following discussion has been adapted from Donald R. Askeland's book titled, *The Science and Engineering of Materials*. Askeland's description are concisely written for anyone who has a minimal background in the study of magnetic properties of materials.

A.   ATOMIC STRUCTURE OF MATERIALS

Atoms comprised of a positively charged nucleus are surrounded by electrons which move about the nucleus in definite states of total angular momentum. Studies have shown that magnetism occuring in transition metals is associated almost entirely with the states of electrons in the third shell of the atomic structure. The ordering of spins of the electrons produces magnetic fields as if charges were in motion.

In most materials there is an identical number of electrons with opposite orientation. Since the polarity of the magnetic field is determined by the direction of the electron spin, equal but opposite spins cancel the magnetic field. Thus no magnetic field exist.

Ferromagnetic materials have high levels of magnetization due to unpaired electrons. Associated with each electron is a magnetic moment. This moment, called the Bohr magneton is equal to [Ref. 14: p. 607]

$$\text{Bohr magneton} = \frac{qh}{4\pi m_e} = 9.27 \times 10^{-24} \text{A} \cdot \text{m}^2$$

where q is the charge on the electron, h is Planck's constant and m_e is the mass of an electron. In an atom, the magnetic moment is due to the orbital angular momentum of the electron as well as the spin of the electron (Figure 33 on page 65). [Ref. 14: p. 608]

Atoms consist of a specific electronic structure characterized by definite quantum state and quantum numbers. Each quantum state can contain two electrons, each having an opposite spin. The magnetic moments of each electron pair in a quantum state are opposed and, consequently, whenever a state is completely full, there is no net magnetic moment. In contrast, any atom of an element with an odd atomic number can have a net magnetic moment from the unpaired electron. However, this is generally not true. In most of these elements, the unpaired electron is a valence electron. Because the
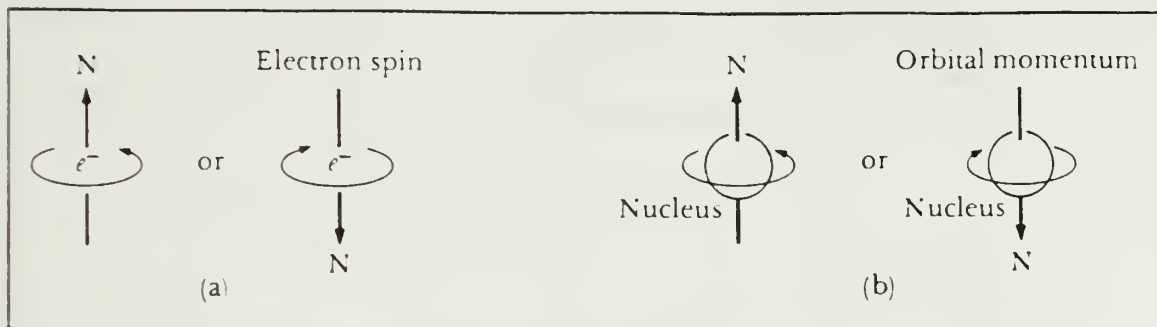
Figure 33. **Origin of Magnetic Dipoles:** (a) The spin of the electron produces a magnetic field with a direction dependent on the quantum number m_s. (b) electrons orbiting about the nucleus create a magnetic field about the atom.

valence electrons from each atom interact in forming the bulk material, the magnetic moments, statistically cancel and no net magnetic moment is associated with the material. Certain elements, such as the transition metals, have an inner energy level that is not completely filled. Figure 34 on page 66 shows the electron spins in the 3d energy level in transition metals for the elements scandium through copper. The arrows indicate the direction of spin. [Ref. 14: p. 609]

The electrons in the 3d level of the remaining transition elements do not enter the shell in pairs. Instead, as in magnanese, the first five electrons have the same spin. Only after half of the 3d level is filled do pairs with opposing spins form. Therefore, each atom in a transition metal has a permanent magnetic moment, dependent in strength to the number of unpaired electrons. Each atom behaves as a magnetic dipole. [Ref. 14: p. 609]

B. DOMAINS

Ferromagnetic behavior is due to unfilled energy levels in the 3d level (for iron, nickel, cobalt). Ferromagnetic materials have their powerful influence on magnetization because of the positive interaction between the dipoles of neighboring atoms. Within the grain structure of a ferromagnetic material, a substructure composed of magnetic domains is produced, even in the absence of an external field. Domains are regions which all of the dipoles are aligned to a common direction. In a material that has not been exposed to an external magnetic field, the individual domains have a random orientation and the net magnetization is zero. [Ref. 14: p. 613]

Metal	3d					4s
Sc	↑					↑↓
Ti	↑	↑				↑↓
V	↑	↑	↑			↑↓
Cr	↑	↑	↑	↑	↑	↑
Mn	↑	↑	↑	↑	↑	↑↓
Fe	↑↓	↑	↑	↑	↑	↑↓
Co	↑↓	↑↓	↑	↑	↑	↑↓
Ni	↑↓	↑↓	↑↓	↑	↑	↑↓
Cu	↑↓	↑↓	↑↓	↑↓	↑↓	↑

Figure 34. Electron Spins of Transition Elements.

The concept of a domain is key to understanding magnetism in materials. Domains are typically very small, measuring about .005 cm or less. Bloch walls, which are boundaries that separate the individual domains measure about 1000 Å thick. These Bloch walls are narrow zones in which the direction of the magnetic moment gradually and continuously changes from that of one domain to that of the next (Figure 35 on page 67). [Ref. 14: p. 613]

When an external field is applied to the material, domains that are already lined up with the field grow at the expense of unaligned domains. In order for the domains to grow, the Bloch walls must move. The imposed magnetic field provides the force required for the walls to migrate. As the strength of the field increases, favorably oriented domains continue to grow and a greater net magnetization occurs. The saturation magnetization, produced when all of the domains are properly oriented, is the greatest amount of magnetization that the material can obtain. [Ref. 14: p. 614]

C. HYSTERESIS LOOP

When the field is removed, the resistance offered by the domain walls prevents re-growth of the domains into random orientations. As a result, many of the domains re-main oriented near the direction of the original field and a residual magnetization, known as the remanence B, persists in the material. The material now acts as a perma-nent magnet. [Ref. 14: p. 614]
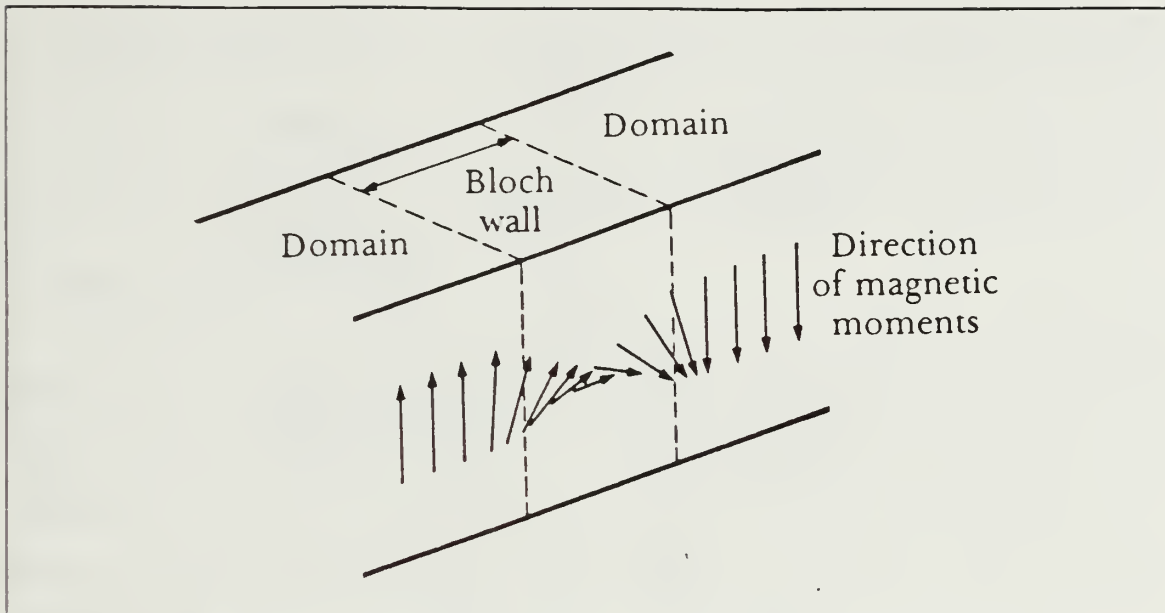
Figure 35.   Magnetic Moments in Adjoining Atoms.

If we now apply a field in the reverse direction, the domains grow with an alignment in the opposite direction. A coercive force H_c is required to force the domains to be randomly oriented. Further increases in the strength of the field eventually align the domains to saturation in the opposite direction. [Ref. 14: p. 615]

As the field continually alternates, the magnetization versus field relationship traces out a hysteresis loop (Figure 36 on page 68). This type of curve applies to all magnetic materials. Materials which have a low coercive force are low energy or soft magnetic materials. High coercive forces occur in rare earth permanent magnets. The power of the magnet is related to the size of the hysteresis loop, or the maximum product of B and H along the B-H curve. The area of the largest rectangle that can be drawn in the second or fourth quadrants of the B-H curve is related to the energy required to demagnetize the magnet. Therefore, large hysteresis loops are desired for permanent magnets, as the loop also represents the amount of energy the magnet can store. [Ref. 14: p. 617]

D. MAGNET DEVELOPMENT

Development of strong permanent magnets, often said to be magnetically hard, is aimed at improving both the magnetic permeability and the stability of the domains. Improved permanent magnets are produced by making the grain size so small that only
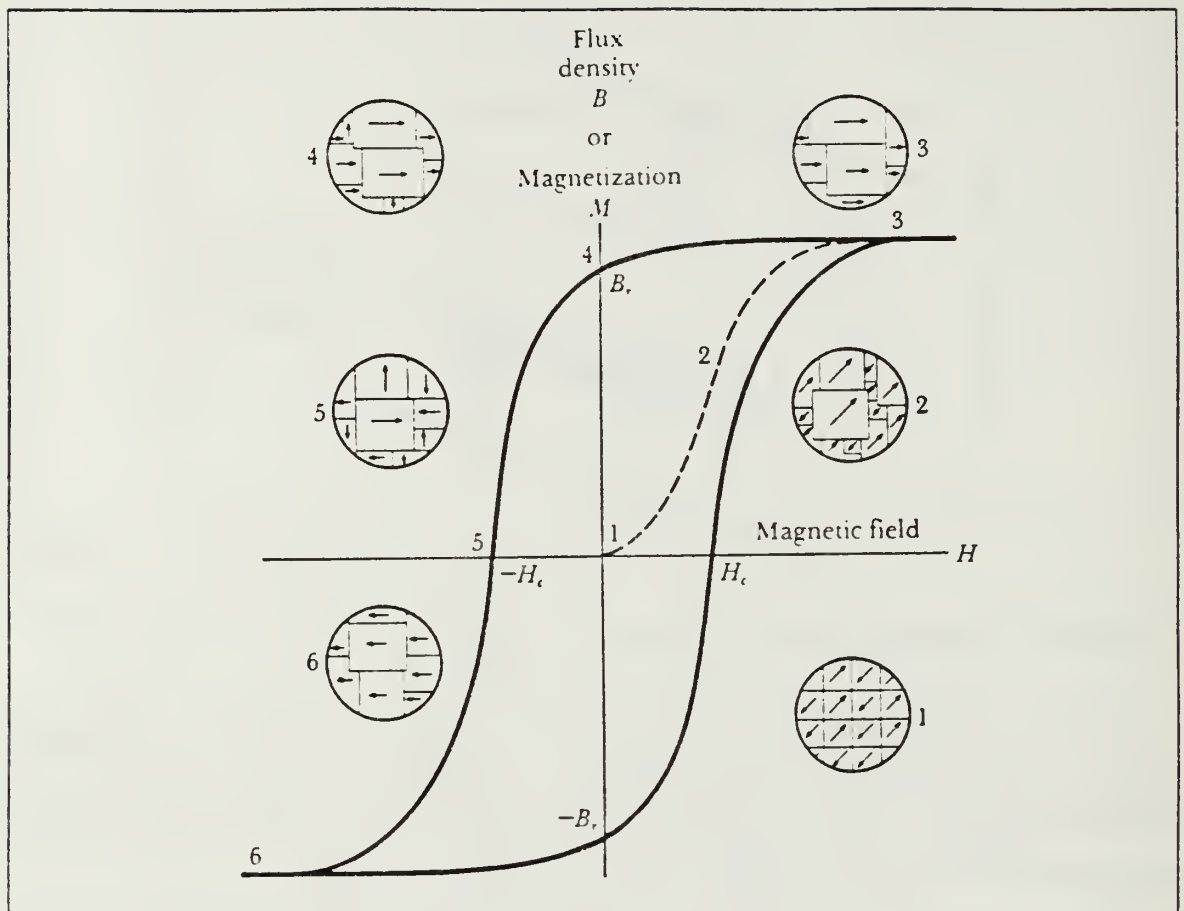
Figure 36. The Ferromagnetic Hysteresis Loop: showing the effect of the magnetic field on inductance or magnetization. The dipole alignment leads to saturation magnetization, point 3, a remanence, point 4, and a coercive force, point 5.

one domain is present in each grain. Now the boundaries between domains are grain boundaries rather than Bloch walls; the domains can only change their orientation by rotating, which requires greater energy than domain growth. [Ref. 14: p. 621]

Two techniques are used to produce these magnetic materials, phase transformations and powder metallurgy. Alnico, one of the most common of the complex metallic alloys, has a single-phase BCC structure at high temperatures. But when Alnico slowly cools below 800 °C, a second BCC phase rich in iron and cobalt precipitates. This second phase is so fine that each precipitate particle is a single domain, producing a very high remanence, coercive field, and power. Often the alloys are permitted to cool and transform when in a magnetic field to align the domains as they form. [Ref. 14: p. 621]

A second technique. powder metallurgy is used for another group of metallic alloys, including samarium-cobalt. The brittle intermetallic is crushed and ground to produce a fine powder in which each particle is a domain. The powder is then compacted when in an imposed magnetic field to align the powder domains. Careful sintering to avoid growth of the particles produces a solid powder metallurgy magnet. [Ref. 14: p. 621]

E. TEMPERATURE EFFECTS

When the temperature of a ferromagnetic material is increased, the added thermal energy reduces the magnetic permeability or magnetization and permits the domains to become randomly oriented. Consequently, magnetization, remanence and the coercive field are all reduced at high temperatures. If the temperature exceeds the critical Curie temperature, magnetic properties of the material no longer exists. The Curie temperature corresponds to a threshold required to destroy the ordering of electron spins, so that the the permanent dipoles in each cell no longer exist. The Curie temperature depends on the type of magnetic material and can be changed by alloying elements. Two common ferromagnetic materials are iron and cobalt. Each has a Curie temperature of 770 °C and 1131 °C respectively. [Ref. 14: p. 619]

F. RADIATION EFFECTS

Radiation effects have caused increasing concern in recent years. Experiments conducted on present commercially-available permanent magnets have shown no harmful effects on magnetic stability when magnets were subjected to moderate levels of radiation. Magnet technology is at its optimum, and with the improvement to produce very high remanence and coercive field, more and more applications of permanent magnets are in high radiation environments.

APPENDIX B. GLOSSARY OF TERMS

The following list of common terms associated with magnetic properties of materials are provided to aid the reader. The publication *Permanent Magnet Guidelines* by Magnetic Materials Producers Association is the source from which the following terms were originated:

B, magnetic induction, is the magnetic field induced by a field strength, H, at a given point. It is the vector sum, at each point within the substance, of the magnetic field strength and resultant intrinsic induction. Magnetic induction is the flux per unit area normal to the direction of the magnetic path.

B_d **, remanent induction,** is any magnetic induction that remains in a magnetic material after removal of an applied saturating magnetic field, H_s. (B_d is the magnetic indcution at any point on the demagnetization curve; measured in gauss.)

B_d/H_d **, energy product,** indicates the energy that a magnet material can supply to an external a magnetic circuit when operating at a point on its demagnetization curve; measured in mega-gauss-oersteds.

$(B_d/H_d)_{max}$ **, maximum energy product,** indicates the maximum intrinsic induction possible in a material.

B_i **, intrinsic induction,** is the contribution of the magnetic material to the total magnetic induction, B. It is the vector difference between the magnetic induction in the material and the magnetic induction that would exist in a vacuum under the same filed strength, H. This relation is expressed by the equation:

$$B_i = B - H$$

where B_i = intrinsic induction in gauss; B = magnetic induction in gauss; H = field strength in oersteds.

B_m , **remanent induction,** is the magnetic induction that remains in a magnetic material after magnetizing and conditioning for final use; measured in gauss.

$B_m H_m$, **energy product,** indicates the energy that a magnet material can supply to an external magnetic circuit when operating at the point ($B_m H_m$); measured in mega-gauss-oersteds.

B_r , **residual induction (or flux density),** is the magnetic induction corresponding to zero magnetizing force in a magnetic material after saturation in a closed circuit; measured in gauss.

H, **magnetic field strength, (magnetizing or demagnetizing force),** is the measure of the vector magnetic quantity that determines the ability of an electric current, or a magnetic body, to induce a magnetic field at a given point; measured in oersteds.

H_c , **coercive force, of a material** is the demagnetizing force corresponding to zero magnetic induction, B, in a magnetic material after saturation; measured in oersteds.

H_{ci} , **intrinsic coercive force,** of a material, indicates its resistance to demagnetization. It is the demagnetizing force corresponding to zero intrinsic induction in a material after saturation; measured in oersted.

H_d , is that value of H corresponding to the remanent induction, B_d; measured in oersteds.

H_m , is that value of H corresponding to the remanent induction, B_m; measured in oersteds.

T_c , **Curie temperature,** is the transition temperature above which a material loses its permanent magnet properties.

μ, **permeability,** is a general term used to express various relationships between magnetic induction, B, and the field strength, H.

ϕ, **magnetic flux,** is a measurable concept that evolved in an attempt to describe the "flow" of a magnetic field.

closed circuit condition exist when the external flux path of a permanent magnet is confined within high permeability material.

demagnetization curve is the second (or fourth) quadrant of a major hysteresis loop. Points on this curve are designated by the coodinates B_d and H_d.

fluxmeter is a galvanometer that measures the change of flux linkage with a search coil.

hysteresis loop is a closed curve obtained for a material by plotting (usually to rectangular coordinates) corresponding values of magnetic induction, B, for ordinates and magnetizing force, H, for abscissa when the material is passing through a complete cycle between definite limits of either magnetizing force, H, or magnetic induction, B.

major hysteresis loop of a material is the closed loop obtained when the material is cycled between positive and negative saturation.

open circuit condition exist when a magnetized magnet is by itself with no external flux path of high permeability material.

permanent magnet is a body that is capable of maintaining a magnetic field at other than cryogenic temperatures with no expenditure of power.

magnetic saturation of a material exists when an increase in magnetizing force, H, does not cause an increase in the intrinsic magnetic induction, B, of the material.

search coil is a coiled conductor, usually of known area and number of turns, that is used with a fluxmeter to measure the change of flux linkage with the coil.

APPENDIX C.   ITS OVERVIEW

The Integrated Tiger Series of Electron/Photon Transport codes (ITS) is the most widely used particle transport code in the world. The code package was developed to incorporate eight individual codes which were developed over the period from 1968 to 1981. All the codes are based on the original ETRAN model developed by M. Berger and D. Seltzer. The ITS code system consists of four primary code packages [Ref. 12: p. 9]:

      XDATA: The electron and photon cross section data file.

       XGEN: The cross section generation program.

          ITS: The Monte Carlo program file.

    UPEML: A machine portable update emulator.

    The heart of the ITS is the program library file ITS, which contains the eight Monte Carlo programs plus system directives for the CRAY, IBM, VAX, and CDC operating systems. The update emulator program UPEML creates the various Monte Carlo codes for a given system with any corrections to those codes that may be desired. The output fortran source code from UPEML is then compiled and stored as an executable module. Program XGEN generates the problem specific cross section data tape using file XDATA for referenced inputs and a user defined input file. The Monte Carlo codes then read in the cross section tape and process the user defined problem.

    One of the eight ITS codes is CYLTRAN, which simulates the transport of particle trajectories through a three-dimensional multimaterial cylinder. For this project only the CYLTRAN code was required. As an ITS user the following steps are required to execute an ITS run:

1. Generate a cross section tape based on the different type of materials contained in the cylindrical geometry of a problem.

2. Create an input file which list all the input parameters required to calculate desired outputs.

3. Submit the input file and the generated cross section tape to the ITS Monte Carlo codes to execute a run.

Table 12 on page 74 is a sample input file to generate the cross section tape for the materials in a cylindical geometry. Each material line represents a different medium in the cylinder. Percentages of each material in a compound and its density must be specified. Single element lines such as Cu, has its density stored in ITS and is automatically entered into the simulation.

Table 12. SAMPLE INPUT FILE TO CREATE A CROSS SECTION TAPE

```
Energy 79.0
Material Cu .04 Ni .07 W .89 Density 17.1
Material Cu
Material N .80 O .20 Gas Density .001226
Material Li .72 F .28  Denstiy 2.69
TITLE
    79 MeV Cross Section for Prod Tgt, Air and LiF
```

Once a cross section tape is generated, an input file with the parameters design for a particular simulation must be created. Table 13 on page 76 is a sample input file to execute an ITS run. The keywords at the beginning of each line are relatively self-explanatory. However, few keywords and their numerical parameters require some explanation to fully understand their importance. These few keywords and their explanation are listed [Ref. 12: pp. 21-23]:

Geometry This keyword sets up the cylindrical geometry of the problem into input zones, where in this case there are seven input zones. Each line of numerical parameters following the keyword describes the dimensions of each zone. Figure 37 on page 77 is a graphic representation of the seven input zones. Note that input zone seven is divided into 10 subzones. This figure represents the half section of a problem cylinder where the z-axis is the axis of the beam center. Figure 37 on page 77 is also the geometrical model used at LLNL. The fifth column of numerical parameters corresponds to the material line as listed in the sample input file in Table 12.

Electron/Photon-Escape This keyword tallies the number of incident electrons and photons that escapes the cylindrical geometry, either latterally or transmitted through.

NBINE tallies the escaped electron/photons in specified energy bins.

NBINT tallies them in angular bins.

Electron/Photon-Flux This keyword tallies the energy deposition of electrons and photons in the subzones described in the keyword geometry.

Histories This keyword represents the number of primary particle histories to follow as it transport through each medium in the cylinder.

Using the input file in Table 12 to generate a cross section tape and executing the input file in Table 13 on page 76 with this tape, a simulation run measuring gamma and electron dose deposited on Li_2F material (TLD chips used at LLNL) will be executed. Table 14 on page 78 is a sample output file used to plot radiation dosage patterns of various materials. This file was generated from the energy deposition output section created by ITS.

Table 13.   SAMPLE OF AN INPUT FILE TO EXECUTE ITS

```
Echo 1
TITLE
   Mat:Tgt,Cu,air,LiF   R = .75cm   D = 78.7cm   His:10000   E = 79MeV
Electrons
Energy 79.0
Cutoffs .1 .1
Position 0.0 0.0 0.0
Radius 0.75
Direction 0.0 0.0
Geometry 7
        0.000       0.254       0.000       0.944       1
        0.000       0.254       0.944       3.492       2
        0.000       0.254       3.492      10.000       3
        0.254       1.054       0.000       3.492       2
        0.254       1.054       3.492      10.000       3
        1.054      78.700       0.000      10.000       3
       78.700      79.000       0.000      10.000       4   1   1   10
Electron-Escape
   NBINE 23 User
        75. 70. 60. 55. 50. 45. 40. 35. 30.
        25. 20. 15. 10. 8. 7. 6. 5. 4. 3. 2. 1.
        .6 .1
   NBINT 16 User
        1.0 2.0 3.0 4. 5. 6. 7. 8. 9. 10.
        15. 20. 30. 45. 90. 180.
Photon-Escape
   NBINE 23 User
        75. 70. 60. 55. 50. 45. 40. 35. 30.
        25. 20. 15. 10. 8. 7. 6. 5. 4. 3. 2. 1.
        .6 .1
   NBINT 16 User
        1.0 2.0 3.0 4. 5. 6. 7. 8. 9. 10.
        15. 20. 30. 45. 90. 180.
Electron-flux 1 10
   NBINE 10
Photon-Flux 1 10
   NBINE 10
Histories 10000
```

Figure 37. Graphic Representation of the Keyword Geometry: where heavimet = 1, copper = 4, air = 3,5,6 and the absorbing material = 7.

Table 14. SAMPLE OF A RADIATION DOSAGE PATTERN OUTPUT FILE

DISTANCE (CM)	PRIMARIES (GRads/Coul)	GAMMAS (GRads/Coul)	TOTAL (GRads/Coul)
0.5000	0.0114 54	0.0648 25	0.0835 20
1.5000	0.0081 56	0.0470 14	0.0557 15
2.5000	0.0165 22	0.0377 11	0.0535 12
3.5000	0.0244 13	0.0430 12	0.0657 7
4.5000	0.0260 16	0.0269 12	0.0527 9
5.5000	0.0183 20	0.0238 8	0.0419 10
6.5000	0.0161 10	0.0227 12	0.0374 9
7.5000	0.0169 20	0.0211 9	0.0381 8
8.5000	0.0194 9	0.0188 9	0.0371 4
9.5000	0.0185 7	0.0150 7	0.0315 6

LIST OF REFERENCES

1. White, R.M., "Opportunities in Magnetic Materials," *Science*, Volume 229, Number 4708, 5 Jul 1985.

2. Brown, R.D., Bush, E.D. Jr., Hunter, W.T., "Radiation Effects of Protons on Samarium-Cobalt Permanent Magnets," LA-9437-MS, Jul, 1982.

3. Colella, N.J., "Effects of Radiation of Rare-Earth Permanent Magnets (REPMs), LLNL Research Memo, RM 86-27, 16 Dec 1986.

4. Coninckx, F., "Radiation Effects on Rare-Earth Cobalt Permanent Magnets," CERN SPS TIS-RF IR 83-07, 14 Feb 1983.

5. Blackmore, E.W., "Radiation Effects of Protons on Samarium-Cobalt Permanent Magnets," IEEE Trans Nuc Sci, (USA) NS-32, 3669-3671, Oct, 1985.

6. Cost, J.R., "Radiation Effects in Rare-Earth Permanent Magnets," LANL Material Science Division, Nov, 1986.

7. Wallace, W.E., Private Communication to N. Colella, LLNL, Dec, 1986.

8. Meyer, P., Fong, H., "Bremsstrahlung Dose Measurement in 0° Cave," LLNL Memo, 10 Apr 1987.

9. Kulke, B., Palomar, J., "Permanent Magnet Radiation Hardness Tests at the 100 MeV Linac: Preliminary Results," LLNL Research Memo, RM 88-16, 01 Mar 1988.

10. Palomar, J.V., Colella, N.J., "Effects of Radiation on Rare-Earth Permanent Magnets Validation Program Proposal, Electronic Support/ Data Acquisition System, LLNL Research Memo, RM 87-1, 01 Jan 1987.

11. McClure, J.C. and Schroder, K., "The Magnetic Barkhausen Effect," *CRC Critical Reviews in Solid State Science*, Jan, 1976.

12. Halbleib, J.A., Mehlhorn, T.A., *ITS: The Integrated Tiger Series of Coupled Electron Photon Monte Carlo Transport Codes*, Sandia National Laboratories Report SAND84-0573, Nov, 1984.

13. Segre, E., *Nuclei and Particles*, W.A. Benjamin, Inc., 1977.

14. Askeland, D.R., *The Science and Engineering of Materials*, Brooks Cole Engineering Division, 1984.

BIBLIOGRAPHY

Buschow, K.H., *New Permanent Magnet Materials*, Elsevier Science Publishers B.V., 1986.

Kittel, C., *Introduction to Solid State Physics*, John Wiley and Sons, Inc., 1967.

Knoll, G.F., *Radiation Detection and Measurement*, John Wiley and Sons, Inc., 1979.

Koch, H.W. and Motz, J.W., "Bremsstrahlung Cross-Section Formulas and Related Data," Rev Mod Phys Vol 31, Nr 4,1959.

Marshall, T.C. *Free-Electron Lasers*, Macmillan Publishing Company, 1985.

Mathews, J.L. and Owens, R.O., "Accurate Formulae for the Calculation of High Energy Electron Bremsstrahlung Spectra," Nuc Inst and Methods III, 1973.

Swanson, W.P., *Radiological Safety Aspects of the Operation of Electron Linear Accelerators*, International Atomic Energy Agency, 1979.

INITIAL DISTRIBUTION LIST

10. LTC Edward Pogue   1
    Strategic Defense Initiative Office
    Directed Energy
    Pentagon
    Washington, D.C. 20301-7100

11. Dr. Carole Johnson   1
    B119, Bldg. 245
    National Bureau of Standards Lab
    Gaithesburg, MD 20899

12. Dr. Sam Penner   1
    B119, Bldg. 245
    National Bureau of Standards Lab
    Gaithesburg, MD 20899

13. Dr. Phillip Sprangle   1
    Plasma Physics Division
    Naval Research Lab
    Washington, D.C. 20375-5000

14. Dr. Cha-mei Tang   1
    Plasma Physics Division
    Naval Research Lab
    Washington, D.C. 20375-5000

15. Prof. John E. Walsh   1
    Wilder Laboratory
    Department of Physics
    Dartmouth College
    Hanover, NH 03755

16. Dr. Bertrand Hui   1
    Naval Surface Warfare Center
    White Oak Laboratory
    Silver Spring, MD 20903-5000

17. Dr. K.-J. Kim   1
    Lawrence Berkeley Laboratory
    University of California
    Berkeley, CA 94702

18. Dr. Klaus Halback   1
    Lawrence Berkeley Laboratory
    University of California
    Berkeley, CA 94702

19. Dr. Robert A. Meggar   1
    Code 4750
    Naval Research Laboratory
    Washington, D.C. 20375-5000

20. LCDR Robert J. Ross   1
    Strategic Forces
    Defense Nuclear Agency
    Washington, D.C. 20305

21. Dr. John Halbleib   1
    Division 1231
    Sandia National Laboratories
    P.O. Box 5800
    Albuqerque, NM 87185

22. LT Henry B. Luna   6
    2554 W San Gabriel Ave.
    Fresno, CA 93705